

**The Effect of Superheat on  
Liquid Droplets in a Supersonic Freestream**

by  
Aaron W. Newman

A Thesis  
Submitted to the Faculty  
of the  
WORCESTER POLYTECHNIC INSTITUTE  
in partial fulfillment of the requirements for the  
Degree of Master of Science  
in  
Mechanical Engineering  
April 1999

Approved:

Dr. James C. Hermanson, Major Advisor  
Dr. William W. Durgin, Thesis Committee member  
Dr. David J. Olinger, Thesis Committee member  
Dr. Nikolaos A. Gatsonis, Graduate Committee Representative

## Abstract

The effect of superheat on the disruption of liquid droplets in a compressible gas flow was investigated experimentally in a small-scale, supersonic wind tunnel. Aerodynamically generated ethanol droplets of an average diameter of 0.1 mm were injected via a normal sonic jet into a Mach 1.8 freestream. Both nonsuperheated and superheated droplets were injected with initial Weber numbers of approximately 700. The droplets and flow structure were photographed using the shadowgraph method. The relatively high momentum of the liquid droplets typically caused them to pass out of the sonic jet structure. Nonsuperheated droplets showed no signs of disrupting after traveling over 200 mm downstream from the injection point. Only droplets with injection temperatures above the predicted boiling point at tunnel freestream static pressure (48° C) showed signs of disruption, typically after they left the sonic jet structure (30 to 100 mm downstream of the injection point). Droplets in this range of temperatures appeared to begin to boil from the downstream side of the droplet, shedding a vapor cloud before disrupting completely in the chaotic mode. Droplets with temperatures above the boiling point at the exit plane of the sonic jet began to disrupt in the chaotic mode almost instantly (within 1 exit nozzle diameter).

## **Acknowledgements**

The author would like to thank Dr. James Hermanson for his guidance and expertise in this study. Without his suggestions and previous work, this research would not have born fruit. Thanks also go to Dr. William W. Durgin, Dr. David J. Olinger, and Dr. Nikolaos A. Gatsonis for taking the time to serve on the thesis defense committee. A special thanks goes to the University of Connecticut Mechanical Engineering Department, for the loan of the argon spark gap generator.

Additional thanks go to Mr. Steve Derosier and Mr. Bob Taylor, whose help in modifying the tunnel and constructing nozzles was invaluable, especially for the epoxy molding technique. Finally thanks go to everyone who helped with suggestions, support and assistance while this research was being conducted: Ken Desabrais, Frank Weber, Pam St. Louis, Peggy Boucher, Niel Norum, and Marty Schwalm.

## Table of Contents

Abstract	ii
Acknowledgements	iii
Table of Contents	iv
List of Figures	vi
List of Tables	viii
Nomenclature	ix
1. Introduction	1
1.1 Background	1
1.2 Disruption of a Non-superheated Droplet in a Compressible Flow	3
1.3 Superheated Liquids	8
1.4 Objectives of this research	12
2. Experimental Methods	14
2.1 Supersonic Tunnel	14
2.2 Injection Apparatus	18
2.3 Liquid Heating	23
2.4 Diagnostic Equipment	25
2.5 Run Conditions	31
3. Simple Analysis of Droplet Injection	33
3.1 Concerns	33
3.2 Simple Injection Model	33
3.3 Model Results	35

3.4 Underexpanded Jet	42
4. Results	46
4.1 Sonic Jet Structure	46
4.2 Droplet Path	49
4.3 Droplet Disruption	53
5. Summary	68
References	72
Appendix A: Numerical Code for Droplet Injection	76

## List of Figures

Figure 1.1: Instabilities associated with droplet disruption	4
Figure 1.2: Drops in a Mach 1.1 flow	7
Figure 1.3: Superheat limits	11
Figure 2.1: Tunnel with one side panel removed	15
Figure 2.2: Tunnel assembled and ready for use	16
Figure 2.3: Modified tunnel schematic	17
Figure 2.4: Representative injection nozzles	18
Figure 2.5: Nozzle and Needle assembly	20
Figure 2.6: Needle assembly	21
Figure 2.7: Liquid pre-heating apparatus	24
Figure 2.8: The shadowgraph effect	27
Figure 2.9: The shadowgraph equipment used in the study	28
Figure 2.10: Shadowgraph schematic	29
Figure 3.1: Relative Mach number as a function of droplet size for normal injection in the test section	37
Figure 3.2: Relative Mach number as a function of droplet size for tangential injection at the tunnel entrance	38
Figure 3.3: Weber number for droplets injected normal to the tunnel flow in the test section	40
Figure 3.4: Weber number for droplets injected tangentially at tunnel entrance	41
Figure 3.5: Sonic jet structure	43

Figure 4.1: Jet and shock structure	47
Figure 4.2: Shock and jet structure outlined for clarity	48
Figure 4.3: Composite graph of all droplet positions under non-disrupting conditions	50
Figure 4.4: Typical photo of droplets being injected into Mach 1.8 flow	52
Figure 4.5: Nondisrupting droplets injected into a Mach 1.8 flow	56
Figure 4.6: Nondisrupting and disrupting droplets	58
Figure 4.7: History of a droplet just above the free stream boiling point	60
Figure 4.8: Disrupting droplets	61
Figure 4.9: Downstream distance range from first to last droplet disruption	63
Figure 4.10: Total distance range from first to last droplet disruption	64
Figure 4.11: Penetration distance range from first to last droplet disruption	65

## **List of Tables**

Table 3.1: Centerline flow-field conditions in the underexpanded jet	44
Table 4.1 Superheat conditions of data	54

## Nomenclature

$\mathbf{a}$	Droplet acceleration
$a$	Redlich-Kwong parameter
$b$	Redlich-Kwong parameter
$Bo$	Bond number
$C$	Collection of constant terms
$C_D$	Discharge coefficient
$d$	Actual orifice diameter
$d_D$	Droplet diameter
$d^*$	Effective orifice diameter
$D_o$	Initial droplet diameter
$\Delta E$	Change in illumination
$F_D$	Force on droplet
$H_{top}$	Penetration of the normal jet, measured from the tunnel wall to the Mach disk
$K_D$	Drag coefficient
$L$	Characteristic length
$M_j$	Mach number of normal jet at exit plane
$M_{rel}$	Relative Mach number between droplet and freestream
$M_s$	Mach number of tunnel flow downstream of bow shock
$M_\infty$	Mach number of free-stream tunnel flow
$Oh$	Ohnesorge number

$P$	Absolute pressure at the superheat limit
$P_c$	Critical pressure
$P_j$	Static pressure of normal jet at exit plane
$P_s$	Static pressure of tunnel after bow shock
$R$	Gas constant
$s$	Droplet path-length
$t_b$	Actual disruption time
$T$	Liquid temperature
$T_b$	Characteristic non-dimensional disruption time
$T_c$	Critical temperature
$T_D$	Temperature of droplet
$T_j$	Temperature of normal jet at exit plane
$T_s$	Static temperature of tunnel after bow shock
$T_{SL}$	Superheat limit temperature
$u_r$	Relative gas velocity
$V$	Velocity
$V_D$	Velocity of droplet
$V_{rel}$	Relative velocity of droplet and freestream
$V_D$	Volume of droplet
$We$	Weber number
$x$	Droplet downstream position
$y$	Droplet penetration

$\varepsilon$	Ratio of the density of the gas phase to the liquid phase
$\mu$	Viscosity
$\rho$	Density
$\rho_A$	Density of the airflow
$\rho_D$	Density of droplet
$\sigma$	Surface tension
$\sigma_l$	Surface tension of the test liquid

# **1. Introduction**

## **1.1 Background**

Recently there has been a revived interest in the supersonic injection of liquids, particularly with respect to fuel injection techniques for such hypersonic programs as the X-33 and hypersonic missiles. These designs require airbreathing engines capable of supersonic combustion. The scramjet (supersonic combustion ramjet), appears at present to be the only practical engine for these types of applications since it is able to produce useful thrust at hypersonic flight Mach numbers, using supersonic flow through the combustor. There is particular interest in hydrocarbon-fueled scramjet engines, whose dense, non-cryogenic, easily storable fuels are especially attractive for many volume-critical missions. The scramjet concept itself is fairly old, and was the subject of studies throughout the 1960s and again in the 1980s.

The effective disruption and mixing of hydrocarbon fuels in a supersonic flow is a topic of great importance for the successful development of these high-speed missions. Three key issues govern the performance of the liquid injection process in a scramjet engine, they are: the penetration of the fuel into the free-stream, the atomization of the injected fuel drops, and the level of fuel/air mixing. [1] It is important for the fuel to penetrate effectively into the free-stream so that the combustion process produces an even temperature distribution. If the fuel does not penetrate sufficiently into the free-stream, the combustion will mostly occur along the surface of the combustor (or injector rake), causing inefficient combustor operation and increased cooling problems. Rapid atomization of the fuel is also required for efficient combustion. Increased atomization of

the liquid fuel results in increased fuel/air mixing which allows a higher percentage of the fuel to be burnt in the short time before the entire mixture passes out of the combustor (generally on the order of 1 ms).

It has been hypothesized that superheated fuels may disrupt faster, and more uniformly than fuels injected under conventional conditions. Using superheat may affect atomization and fuel/air mixing [2]. High (or possibly even low) levels of superheat could be used to cause flash vaporization (the explosive vaporization of a liquid at temperatures above its boiling point) of the fuel before combustion. Therefore a correlation between the level of superheat and disruption rate could be of great help in the development of the scramjet.

One additional factor concerning scramjet operation that is affected by the use of superheated fuels has been termed the 'cold-start' issue. Typical hypersonic designs often utilize fuel circulation through the skin of the aircraft (and sections of the engine) to cool the structural materials sufficiently to allow operation at the high temperatures produced by skin friction at these speeds. The same process is also used to pre-heat the fuel before being burned in the combustor. This allows pre-vaporized fuel to be used, which would be the preferred method of operating a combustor under these conditions. For the case of a hypersonic vehicle that begins scramjet operation at low supersonic or subsonic velocities, the skin temperature may not be sufficient to vaporize the fuel. At this point liquid fuel would be injected into the combustor. Under these circumstances superheated fuels may be a more attractive alternative to simple liquid fuels.

## **1.2 Disruption of a Non-superheated Droplet in a Compressible Flow**

A non-superheated droplet in supersonic flow under normal conditions deforms due to several different and competing mechanisms. One mechanism is due to the difference between the velocities of the liquid droplet, the surrounding vapor, and the free-stream gas, which produces a shear instability. This is the Kelvin-Helmholtz instability mechanism [3]. The density variation between these same three phases coupled with the droplet acceleration produces a Rayleigh-Taylor inertial instability [4]. The last major driving mechanism is the result of rapid vaporization and its accompanying evaporative mass flux [3, 5, 6]. Finally the pressure gradient across the droplet caused by passing through a shock can create an instability within the drop, leading to disruption [3]. It should be noted that most previous studies have involved drops under impulsive (passage of a shock past a stationary droplet), or subsonic injection conditions, which differ significantly from conditions found in scramjet fuel injectors. Fig. 1.1 shows these and other instabilities which may cause a droplet to deform in a compressible flow field.

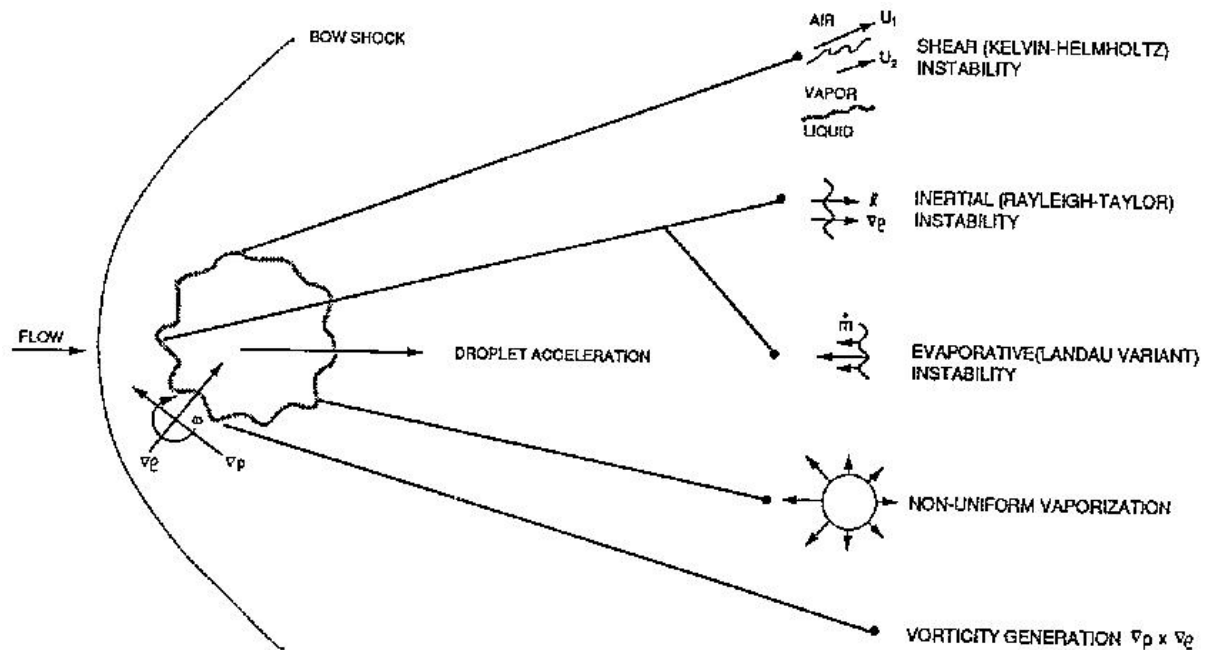


Fig. 1.1 Instabilities associated with droplet deformation [3].

Previous studies have shown that the type and rate of deformation of non-superheated droplets in shock tubes are strongly dependent on two dimensionless parameters. The first of these is the Weber number, which relates the force of deformation on the droplet (characterized by the relative velocity) to the surface tension. The second is the Ohnesorge number, which is a parameter relating viscosity to surface tension.[7]. Mathematically,

$$We = \frac{\rho V^2 L}{\sigma} \quad (1)$$

$$Oh = \frac{\mu}{(\rho \sigma L)^{1/2}} \quad (2)$$

The length is taken to be the droplet diameter. For the Weber number, the density  $\rho$  is of the free-stream gas, as is the velocity  $V$ . For the Ohnesorge number, both the viscosity  $\mu$ , and the density  $\rho$  are of the liquid. A third parameter, the Bond number, relates acceleration to surface tension,

$$Bo = \frac{a \rho L^2}{4\sigma} \quad (3)$$

where the density is also of the liquid drop. The Bond number can be related to the Weber number through the drag coefficient, and fills a similar function in relating the droplet acceleration to its surface tension. The effect of the Ohnesorge number on droplets of the size used for this investigation will not be significant when compared to the Weber number [3, 7], since the Ohnesorge number will not significantly change.

The Weber number by contrast, may potentially undergo significant changes as the droplet's relative velocity changes due to droplet acceleration. This in turn results in large changes in droplet stability. The Ohnesorge number on the other hand, has far smaller changes over the range of flow conditions, and a correspondingly smaller effect on droplet stability.

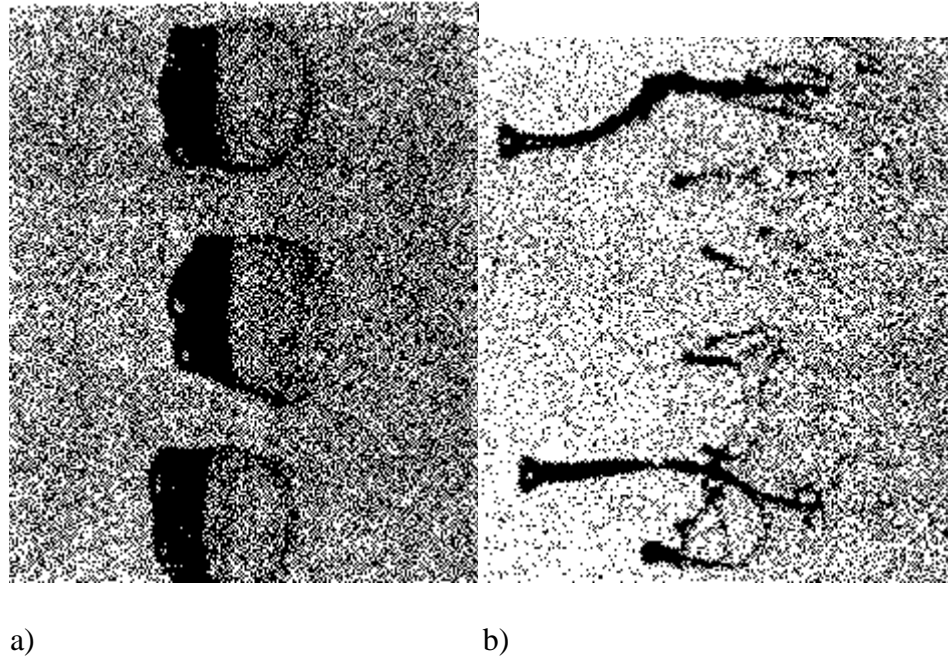
The primary importance of the Weber number on a droplet is to determine whether the droplet will disrupt and in what mode it will disrupt. Previous studies (primarily conducted in shock tubes) have identified many different modes of breakup for a droplet in high speed air flow [7-10]. Droplets are typically stable for Weber numbers less than approximately 10. With higher Weber numbers, a bag mode of breakup occurs, and at still higher Weber numbers (generally above 65 to 100), shattering style breakups [7, 8, 9, 10] are observed. It is also common, depending on the type of diagnostic being used, to observe a mist in the wake of the droplet [8].

Previous studies on the mechanics of the breakdown of a non-superheated liquid droplet under the influence of a supersonic gas flow have predominantly been carried out in shock tubes. Hirahara & Kawahashi conducted studies in a Mach 1.1 shock tube, where droplets of water and silicone oil were generated by an oscillating capillary tube [7]. The droplets formed were in the range of 200 to 500  $\mu\text{m}$ , with Weber numbers from 7 to 100. They report droplets showing no deformation for Weber numbers of 7.1, while deforming under a "bag" mode and "stamen" mode for Weber numbers of 10 and 13 respectively.

In the bag mode, the droplet expands and balloons outward before finally becoming too stretched to hold together, as shown in Fig. 1.2. A droplet deforming by the

stamen mode is shaped into a cone and then a disk which retains the central protrusion of the cone [6]. The droplet then deforms similar to the bag mode, but retaining this central stamen which may remain even after the bag portion of the droplet has fully disrupted.[7]

Fig. 1.2 shows both these modes.



a) b)  
 Fig. 1.2 Drops in a Mach 1.1 flow (from left to right) disrupting in the bag mode (a), and the stamen mode (b) [7].

Tan and Bankoff [10] studied 300  $\mu\text{m}$  to 800  $\mu\text{m}$  diameter mercury drops in a shock tube (1.7 MPa shock pressure). For drops with a Weber number less than 17, the drops simply oscillated and deformed slightly after the passage of a shock. Since droplets typically deform at this Weber number, it may be possible that other conditions contributed to an increase in droplet stability. Drops with Weber numbers above this level experienced rapid explosion in all directions, followed by violent disruption. They also noted that the characteristic non-dimensional time for disruption,  $T_b$  of a droplet deforming via Taylor instabilities is dependent on the Weber number:

$$T_b = 1.16 We^{-1/4} \epsilon^{-1/2} \quad (4)$$

where  $\varepsilon$  is the ratio of the density of the gas phase to that of the liquid phase.[9] Experimentally, the dimensionless breakup time is defined as:

$$T_b = t_b u_r \varepsilon^{1/2} / D_o \quad (5)$$

with  $D_o$  the initial droplet diameter,  $u_r$  is the relative gas velocity, and  $t_b$  is the actual droplet disruption time.

There appears to have been very little previous work describing the effect of Weber numbers significantly higher than 100, as were encountered in this study. It was expected that droplets would continue to deform in a chaotic or shattering style breakup under the high Weber number conditions (approximately 700) seen in this study.

### **1.3 Superheated Liquids**

As mentioned previously, superheat can be used to dramatically increase the rate and violence of a liquid droplet's disruption. A superheated liquid is a liquid existing in a metastable state at a temperature above its normal boiling point. This is usually achieved by raising the liquid temperature above its boiling point in the absence of a suitable nucleation site that would allow boiling to occur. Such sites are usually a liquid-vapor boundary. However due to the porousness of most solid surfaces, trapped gas in pores will also act as nucleation sites in liquid-solid boundaries [11].

The classic method of generating a superheated liquid was introduced by Moore [12], and Wakeshima & Takata [13]. This method involves a tall column filled with a host liquid. The temperature of the column increases from the bottom to the top, but is at

no point above the boiling point of the host fluid. A drop of a test liquid, which is less dense than the column fluid, and small enough that heat transfer is rapid enough to avoid any temperature gradients, is injected at the bottom of the column. As the drop rises through the column, its temperature will rise until it reaches its boiling point. The test liquid will not boil, but will continue to rise in elevation and in temperature.

Eventually the drop will reach a temperature at which it will vaporize explosively. This maximum attainable temperature is referred to as the superheat limit, or cavitation limit. The explosive boiling of a liquid which has reached its superheat limit is quite powerful and occurs over very rapid time scales, with a rate of energy release that exceeds many explosives, including black powder. These explosions occasionally occur in some industrial processes, such as molten metal casting where liquid steel or aluminum may accidentally come in contact with water, and aluminum-uranium fuel rods of a water enclosed nuclear reactor [11].

The reason why superheating is possible stems from the difference between conventional boiling and boiling in a superheated state. For a liquid just above its boiling point, the formation of a vapor phase in the bulk of the liquid is possible, but the small vapor embryos formed are unstable and will most likely collapse upon themselves due to surface tension and condensation. In order for bubbles to grow large enough to disengage themselves from the host liquid, an external vapor phase is required, such as the nucleation sites already described. This external vapor phase is any vapor which contacts the liquid phase, providing nucleation sites for the liquid. These sites feed the forming vapor embryo, allowing it to increase in size beyond the point where surface tension is

able to cause it to collapse. At this point that the liquid is considered boiling, as the vapor bubble rises through the liquid. When a liquid under these conditions starts to boil, the vapor left by the rising bubbles is sufficient to continue the boiling process, providing required nucleation sites. Once the same liquid reaches its superheat limit, the same vapor embryos that failed to become bubbles by conventional boiling, are able to grow to a critical size before being condensed back into a liquid, without the need for an external vapor phase and nucleation sites. At this point the bubble grows at a drastically increased rate, causing the apparent explosion of the liquid, often termed flash vaporization [11].

Reid [11] has correlated many different studies of superheated liquids (using the host liquid/test liquid process described above), and found a trend in the location of the superheat limit as shown in Fig. 1.3. This trend relates  $T_{SL}/T_c$  and  $P/P_c$ . where  $T_{SL}$  is the superheat limit temperature,  $T_c$  the critical temperature,  $P$  the absolute pressure at the superheat limit, and  $P_c$  is the critical pressure. The experimentally determined values of  $T_{SL}$  for the many test liquids fall close to a curve generated by the Redlich-Kwong equation:

$$P = RT \left( \frac{1}{V - b} - \frac{a}{RT^{3/2}V(V + b)} \right) \quad (6)$$

and is shown in Fig. 1.3.  $V$  is the liquid volume,  $P$  the pressure,  $T$  the temperature, and  $R$  the specific gas constant. The parameters  $a$  and  $b$  are functions of the critical temperature and pressure. Using this correlation, the superheat limit can be found for any pure liquid at a given temperature and pressure [11].

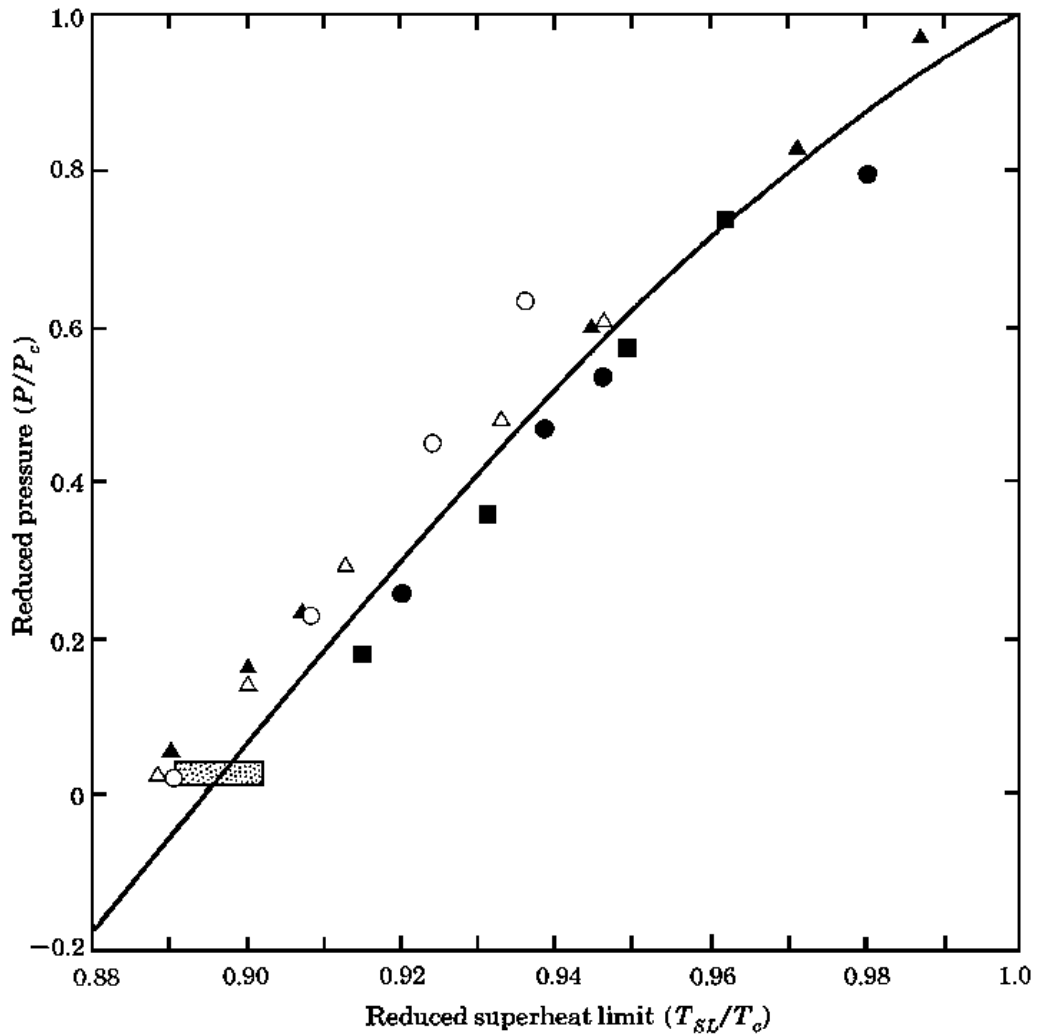


Fig. 1.3 Superheat limits compiled by Reid, shown with the Redlich-Kwong equation (solid line).

Frost [14] conducted a study of the initiation of boiling by directing shock waves at droplets immersed in a test liquid. Relatively large droplets (1 to 2 mm diameter) of ether and isopentane were heated to a temperature below the superheat limit while immersed in glycerol. A spark discharge was used to direct shocks at the droplets. For droplets close to the superheat limit, explosive boiling was triggered. For drops stably

boiling, the interaction with the shock caused the drops to boil unstably, shedding a fine mist of liquid similar to what Hirahara found at high Weber numbers (near 100). Frost also found that explosive boiling in drops interacting with a shock begins on the side of the drop farthest from the shock impact. He further concluded that the pressure rise generated by the shock wave is not responsible for the induced nucleation that causes the explosive boiling, but rather it is the pressure generated in the following expansion which generates the multiple nucleation sites [14]. Other studies have used lasers to raise droplet temperatures above the superheat limit and vaporize explosively [2, 15, 16, 17]. In these studies, explosive evaporation occurs only if the laser was of sufficient energy to raise the droplet temperature (locally or throughout the entire droplet) above the superheat limit.

As mentioned earlier, very few studies have examined the behavior of a superheated liquid droplet in a supersonic flow. Several competing mechanisms are at work due to the supersonic and superheat effects that have been discussed.

#### **1.4 Objectives of this research**

The objectives of this study included the demonstration of the capability to inject discrete liquid droplets of reproducible size into a continuous supersonic flow, and to analytically predict, and if possible determine experimentally, the superheat limit of the test liquid. Also of interest was the effect of superheat on the droplet's behavior, particularly with respect to disruption rate and mode.

Chapter 2 describes the modifications which were made to the tunnel based on the results of the numerical model. It also describes the resulting tunnel performance, as well

as the design and construction of the droplet heating and injection equipment and the diagnostic methods. Chapter 3 will detail the determination of the injection technique which was used. Chapter 4 describes the results of the injection of droplets throughout the transition range to superheat. Concluding remarks and discussion are presented in Chapter 5.

## **2. Experimental Methods**

Superheated droplets were generated differently in this study than in the bubble column experiment described in Chapter 1. The method used here also relies on bringing droplets that are initially below their boiling point above that point without exposing them to nucleation sites, by rapidly lowering the droplet pressure. The temperature of the droplets is regulated prior to injection. As the droplets are suddenly injected into the supersonic tunnel, the pressure falls quickly compared to the droplets' temperature. The lower pressure of the test section lowers the droplet's boiling point below the temperature of the liquid. In this manner the droplet reaches a state of superheat, and since it is exposed to the free-stream (a vapor phase) it will undergo a superheat explosion. A droplet that does not have its boiling point lowered below its temperature, will not explosively vaporize. Rather it will disrupt through conventional processes (such as the Rayleigh-Taylor, Kelvin-Helmholtz, and other instabilities discussed in Section 1) operative in the supersonic flow. It is essential to that the droplet experience a sufficiently rapid pressure drop so that the temperature of the droplet does not significantly decrease [14].

### **2.1 Supersonic Tunnel**

The supersonic wind tunnel used for this study was designed and constructed as a Major Qualifying Project at WPI [18]. The tunnel was constructed to study the acceleration and disruption of liquid droplets injected tangentially at the tunnel entrance.

An evacuated tank attached to the tunnel downstream of the diffuser provides the pressure difference necessary to operate the tunnel. The tunnel inlet is open to the atmosphere. The tunnel was constructed of aluminum, with an 8 in. (20.32 cm) intake height, 0.592 in. (1.5 cm) throat height, and 1 in. (2.54 cm) test section height. A constant width is maintained at all sections of 1 in (2.54 cm), with a 0.25 in (0.635 cm) side wall thickness. The test section is 7 in. (17.8 cm) long, with 5 in. (12.7 cm) quartz windows on both sides, for observation of injected particles. The total length of the tunnel from inlet to the end of the diffuser measures 21.75 in. (55.24 cm). A photograph of the tunnel with one side removed is shown in Fig. 2.1.

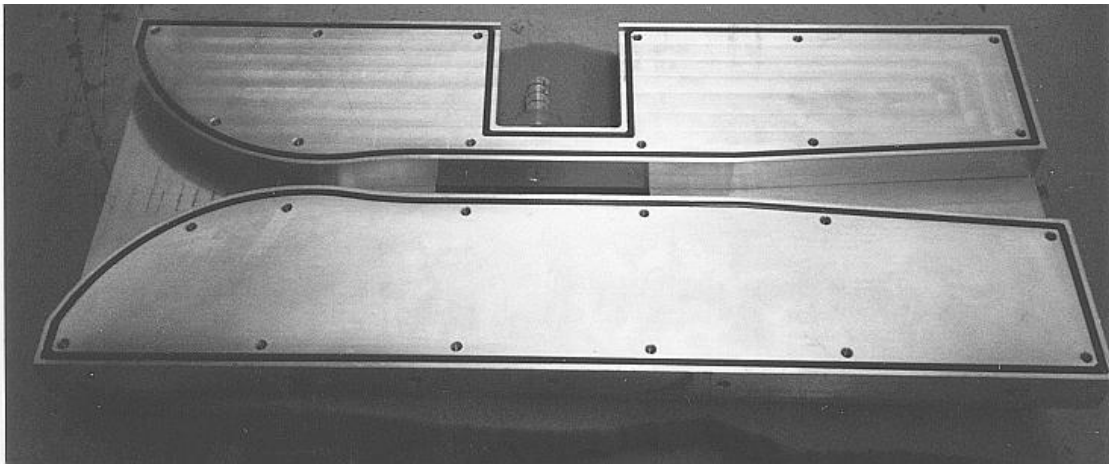


Fig. 2.1 Tunnel with one side panel removed. Flow is from left to right. The dark lines around the edges are the rubber o-rings used to seal the tunnel.

To attach the tunnel to the vacuum tank, an aluminum bracket was constructed that connected to the ball valve on the tank. This bracket allows easy removal of the tunnel for cleaning or other servicing. The removable part is sealed by a rubber o-ring.

The wind tunnel was designed for a nominal Mach number of 2.0 for approximately 30 seconds. Fig. 2.1 shows the tunnel with one of the side panels removed for optical access, and Fig. 2.2 shows the tunnel fully assembled and attached to the vacuum tank, diagnostic equipment and injection apparatus. The vacuum tank is depressurized by a vacuum pump. Approximately 2.5 hours are required using a 5 hp vacuum pump to depressurize the tank from atmospheric pressure to a pressure of 13.5 KPa.

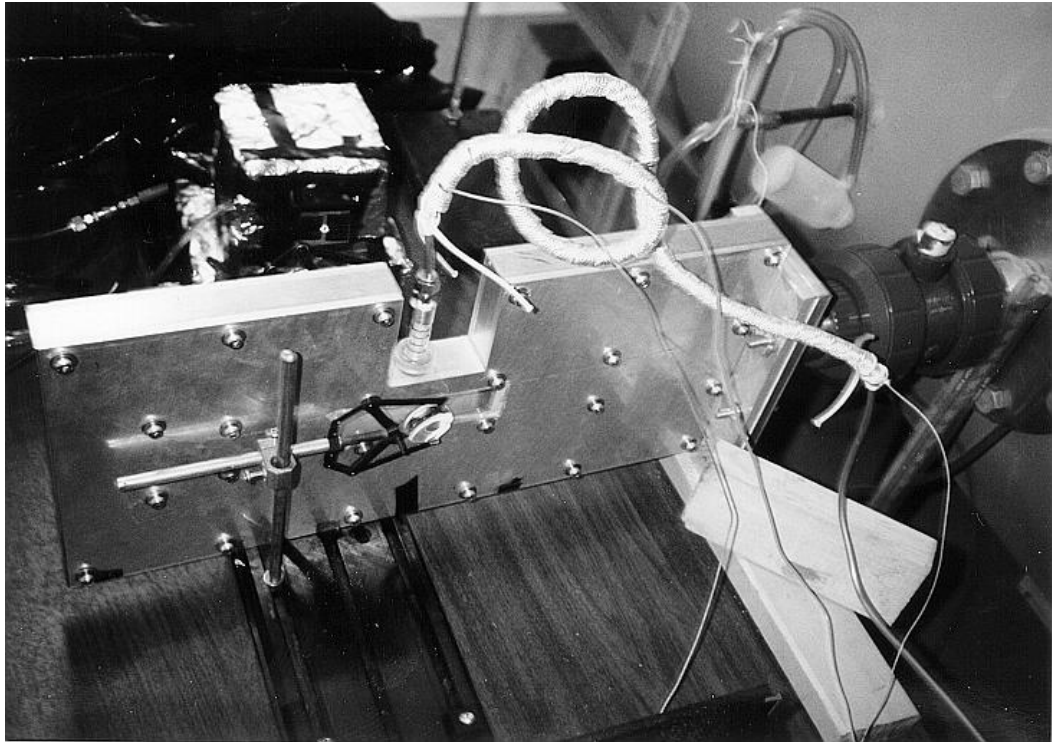


Fig. 2.2 Tunnel assembled and ready for use. Ambient air enters through the left side and exits to the vacuum tank on the right. The liquid heating and injection apparatus is seen attached to the tunnel above the test section. The test section windows can be seen behind the lens in the center of the picture.

As originally designed, the supersonic tunnel was to use tangential droplet injection at the tunnel entrance. As a result of the conclusions drawn from the numerical

analysis (discussed in the next section), the modifications described below needed to be made to the supersonic tunnel to allow normal injection into the test section.

A large piece of the tunnel center section, just above the test section, was cut out, and a hole drilled directly into the top of the test section. This hole is 0.5 in. (1.27 cm) in diameter and located 0.25 in. (0.635 cm) downstream from the start of the test section window. The hole is large enough to accommodate a variety of different sized nozzles and plugs. The nozzles and plugs are all of a similar design and seal against the top of the tunnel with a rubber o-ring. The final nozzle design used for droplet injection is discussed in more detail below. The modified tunnel schematic is shown in Fig. 2.3, and some of the plugs and nozzles used are shown in Fig. 2.4.

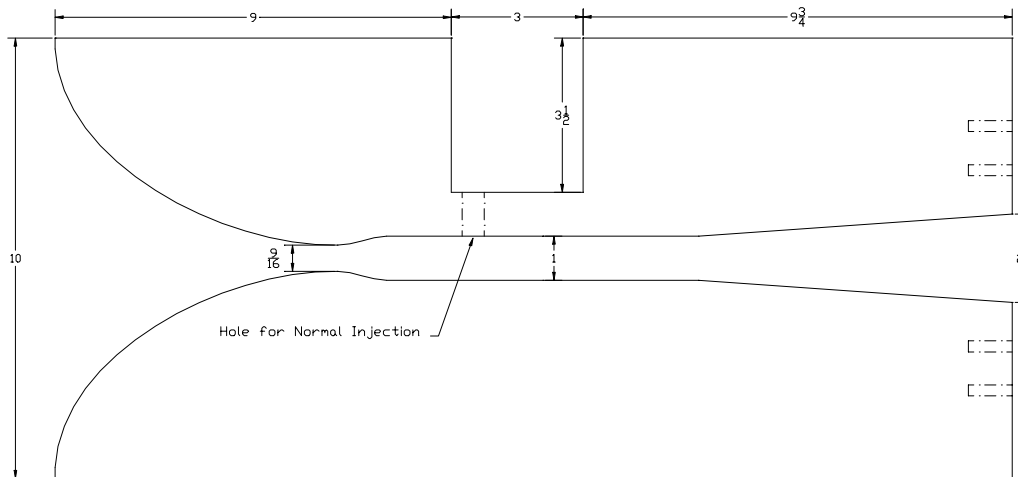


Fig. 2.3 Modified tunnel schematic, flow is from left to right, dimensions in inches.



Fig 2.4 A few of the nozzles used throughout the study. On the left is the metal plug used to seal the hole in the test section. The center nozzle was an early plastic design not used to collect data, the right nozzle is one of the epoxy nozzles of the final design.

## 2.2 Injection Apparatus

The injection apparatus consists of a vessel to store the test liquid, a metering valve to control the flow rate, and a length of copper tubing that connects to the nozzle assembly. The copper supply line can be heated to change the temperature of the liquid. A needle or nozzle assembly used for injection of the liquid into the tunnel is located at the end of the copper tubing.

The critical part of the apparatus is the nozzle/needle assembly at the end of the tubing. The nozzle must inject liquid droplets into the tunnel at a velocity sufficient to penetrate the tunnel boundary layer. It must also generate droplets of a uniform size and accelerate them to the required velocity without disrupting them before their entrance into the tunnel.

A number of injection schemes have previously been used to inject liquid droplets into supersonic flow at high frequency (above 100 Hz). Most have involved either a mechanical means of breaking up a jet, typically a valve or pump capable of a high pulse rate (like a solenoid valve capable of the 100 Hz requirement) [5, 10], or a vibrating orifice or capillary tube [7, 9, 17]. However, in nearly all of those cases, the droplets were injected into the test area prior to the start of supersonic flow, such as in a shock tube. In theory, it should be possible to generate droplets aerodynamically by shearing them off of a small needle or capillary tube inserted into the free-stream. This is the method which was chosen for this study due to its lack of moving parts, low cost, and ease of mechanical assembly as compared to the other two methods.

Several different injection options were considered which involved the direct normal insertion of a hypodermic needle into the test section. These methods proved unacceptable due to two difficulties. At higher liquid flow rates, the pressure gradient drove the liquid into the tunnel flow as a liquid jet, while at lower flow, aerodynamic forces sheared the droplets from the tip of the needle, causing immediate disruption.

A more suitable method was suggested by Green et al. [19], who used converging and converging-diverging nozzles to shear liquid droplets from the ends of capillary tubes. Variations in droplet size can be accomplished by changing the flow rate of the liquid and the air through the nozzle.

The final assembly used the injection supply apparatus described above, which terminated in a 0.0156 in. (0.4 mm) diameter hypodermic needle at the end of the copper tubing. The needle was inserted 0.156 in. (4.0 mm) upstream of the nozzle throat in a 6°

converging nozzle, with throat area of  $0.0069 \text{ in.}^2$  ( $4.45 \text{ mm}^2$ ). This assembly is shown schematically in Fig. 2.5, and photographically in Fig. 2.6. The near-sonic air jet that enters into the test section perpendicular to the tunnel flow both shears droplets from the needle supplying the liquid, and propels them into the tunnel and through the boundary layer. Having negligible velocities at the needle tip, the  $0.1 \text{ mm}$  droplets produced by this method were accelerated to an estimated Mach number of  $0.85$  at the point at which they entered the test section.

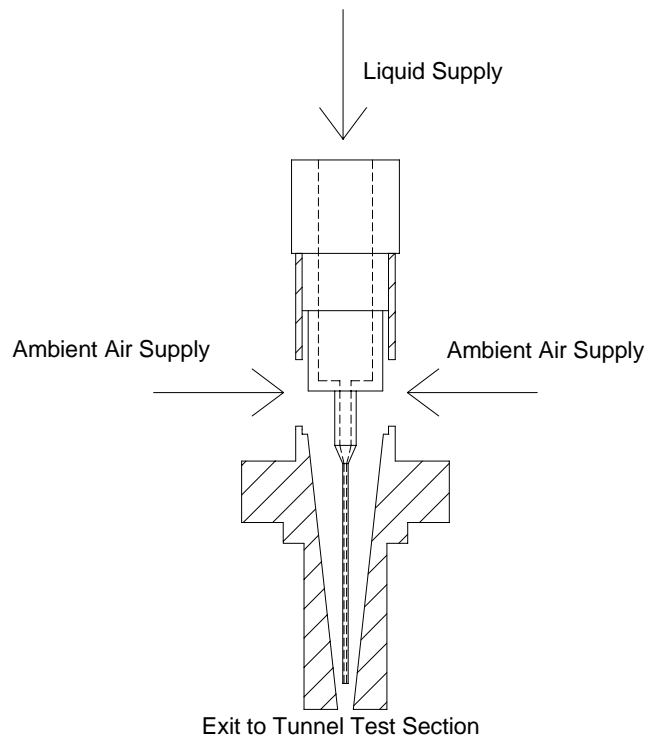


Fig. 2.5 Nozzle and Needle assembly.



Fig. 2.6 The needle assembly (left) shown partially removed from the nozzle assembly (right).

The nozzle section of the assembly contains a plastic inner contour taken from the end of a 50 ml pipette. The outer section of the nozzle was made of 2-ton epoxy molded to fit the hole in the tunnel test section.

Several different injection configurations were tried based on the converging nozzle concept. All used a converging nozzle exiting into the tunnel test section at sonic velocity, with a hypodermic needle mounted in the center. The primary difference between the configurations were the distance upstream of the throat that the needle was placed, and nozzle convergence angle. Due to the long preparation time required to operate the tunnel and the short run times, most of the nozzle configuration tests occurred in static tests outside of the tunnel. For these tests, pressurized air was supplied to the nozzle which exhausted to atmospheric conditions. The liquid supply was pressurized to a pressure equal to, or greater than that of the air supply. The air pressure ratios were

sufficient to allow sonic velocities at the nozzle exit. Air regulators were used to control the pressures of the air and liquid supplies.

Configurations with the needle placed far upstream ( $M \leq 0.1$ , over 5 exit diameters upstream of exit) from the throat to achieve the lowest possible free-stream velocity generated droplets very well, but the droplets were usually disrupted by the time they entered the tunnel. Steeply sloped nozzles also generated droplets well, but the droplets tended to impact the sides of the nozzle and also be disrupted. It was more difficult to generate droplets using gently sloped nozzles with the needle placed close to the throat ( $M \geq 0.5$ , less than 2 exit diameters upstream) since droplet production became much more sensitive to the liquid flow rate. However, these were the only methods which successfully injected droplets into the test section. Droplet quality was confirmed with the shadowgraph method (discussed below).

A metering needle valve was used to control the mass flow rate of the liquid to reliably generate liquid droplets in the tunnel. The volumetric flow rate for the runs using ethyl alcohol was  $0.5 \text{ cm}^3/\text{sec}$  ( $0.031 \text{ in}^3/\text{sec}$ ). To insure a continuous supply of liquid to the tunnel, the lines were pressurized just before the run using building air supply. This priming procedure forced out any air trapped in the end of the needle. It also replaced the cold liquid in the needle with hot liquid from the heated tube (described below).

The average velocity of droplets exiting the needle tip was calculated to be  $10.2 \text{ m/s}$  ( $32.8 \text{ ft/s}$ ) based on the liquid flowrate. Using the droplet acceleration relations developed in Chapter 3, the droplet velocity at the entrance to the tunnel (nozzle exit) was predicted to be  $256.4 \text{ m/s}$  ( $841.2 \text{ ft/s}$ ). Droplet size was very repeatable, however droplet

injection frequency (as revealed by the droplet separation) was not. The average diameter of droplets (ethyl alcohol), measured from the shadowgraph images, was estimated to be 0.1 mm (0.0039 in.), with droplets ranging from 0.08mm to 0.11 mm (0.0031 in. to 0.0043 in.) in diameter. Droplets within a given run exhibited even greater consistency than the study average, nominally less than 0.005mm (0.0002 in.) variance.

### **2.3 Liquid Heating**

The test liquid was heated by use of a resistance heating tape. The tape was wrapped around approximately 2 ft (0.6 m) of the copper supply line upstream of the injection needle. This setup was used to attain liquid temperatures up to 66°C (as measured with a K-type thermocouple located between the heating tape and the supply line). The ethanol supply was heated for a nominal time of at least one hour previous to the run. This is far in excess of the characteristic heating time of ethanol for this geometry, which is approximately 5 minutes.

The priming procedure used to clear the needle of any air bubbles also replaced the unheated ethanol in the needle with heated ethanol from the tubing. This was done at the start of each run, immediately prior to injection into the tunnel, to minimize cooling. The actual temperature of the liquid was measured immediately after the run was completed by injecting a small amount of liquid into a beaker and measuring the temperature with a K-type thermocouple accurate to within 1°C. This is the liquid temperature which was recorded for the run. A second thermocouple was used to measure the temperature of the copper tubing and heating tape to prevent the temperature of the

ethanol in the line from exceeding its boiling point. This limited the maximum temperatures which could be attained by droplets in the tunnel to the value mentioned above of  $66^{\circ}\text{C}$ . Fig. 2.7 shows the heating tape attached to the liquid supply lines, and attached to the tunnel. The purity of the ethanol used was listed as greater than 99%.

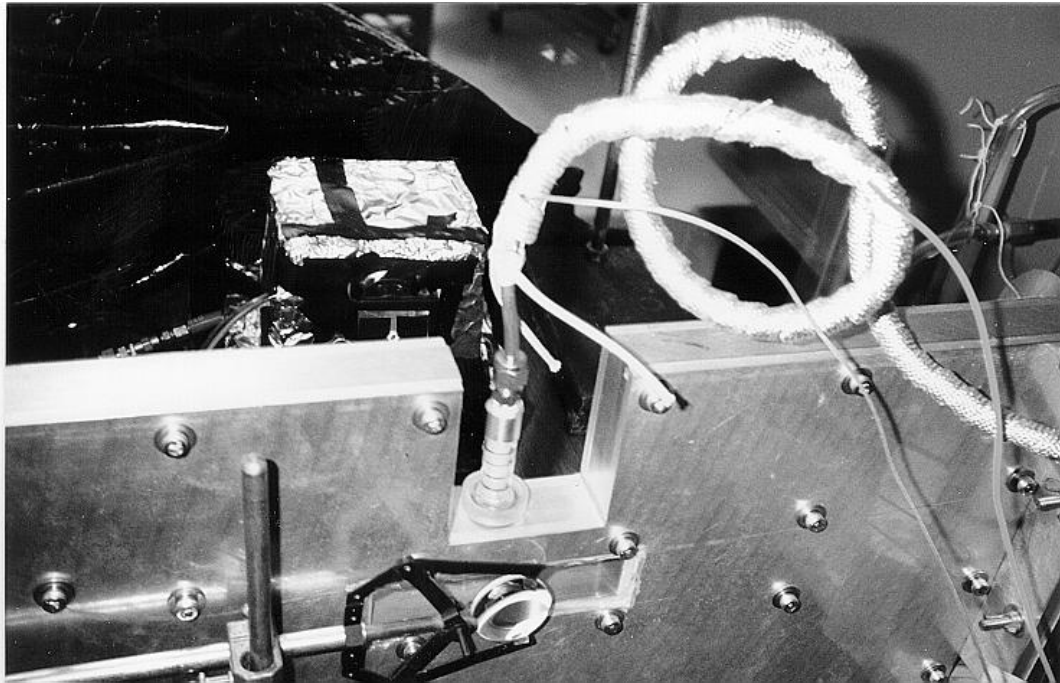


Fig. 2.7 Close-up of the heating tape wrapped around the coiled copper liquid supply line for the injection apparatus.

Droplets existed for a total of  $33\ \mu\text{sec}$  ( $25\ \mu\text{sec}$  in the droplet generator, and an estimated  $8\ \mu\text{sec}$  in the test section), before passing outside of the observable region. Estimates of the time droplets existed in the test section were based off of their vertical penetration into the test section and the calculated initial droplet velocity, neglecting any deceleration in the time span of interest. Calculations were performed to estimate the amount of cooling which the droplet undergoes during this time. As the calculated Biot numbers both in the injection nozzle ( $0.0044$ ) and test section ( $0.00086$ ) were both far

below 0.1, a lumped parameter analysis of the ethanol drop was used [20]. The result of this analysis indicated that the droplet would cool by less than 0.6 °C (1.1 °F), given an initial droplet temperature of 66 °C. As this amount is within the inaccuracy of the temperature measurement, this temperature drop was not taken into account, other than to justify the assumption that the temperature falls more slowly than the pressure, allowing the droplet to reach a superheated state.

## **2.4 Diagnostic Equipment**

The primary diagnostic used in this study to observe droplet behavior was the shadow, or shadowgraph method. Pressure taps and mercury monometers were also used to measure tunnel pressure to allow the determination of the velocity in the test section.

Several different optical methods are used to study compressible flows. Interferometry is sensitive to the actual density change of the fluid flow, schlieren imaging measures the density gradient, and the shadowgraph method measures the second derivative of the density. The shadowgraph method is widely used for studying compressible flows due to the large density changes in such flows. This method is also simpler to implement than the schlieren and interferometry techniques. It is difficult to determine quantitative density measurements via a shadowgraph image, but it is very convenient for gathering qualitative information and quantitative measurements on shock angles, droplet size, and disruption location.

In this method, parallel (or uniformly diverging or converging) light rays are refracted as they pass through the test section of the wind tunnel. Since the index of

refraction is proportional to the density of the medium, light rays passing through sections of the tunnel having differing densities will be refracted at different angles. This causes areas of increased and decreased illumination to be seen on a screen or film placed after the test section, corresponding to regions of different density gradients in the fluid flow, as shown in Fig. 2.8. Although in principle the actual second derivatives of density may be calculated by using:

$$\Delta E = \frac{\partial^2 \rho}{\partial^2 y} + \frac{\partial^2 \rho}{\partial^2 z} \quad (7)$$

where  $\Delta E$  is the change in illumination, the method is more commonly used qualitatively to measure such features as shock angle and jet heights [21]. It should be noted that most features will be shown as a dark line followed by a bright line, or vice versa [21]. In this study the shadowgraph method was used to determine droplet position and level of disruption, shock wave location, jet penetration, and boundary layer thickness. The mode of disruption was studied by visual observation from shadowgraph images.

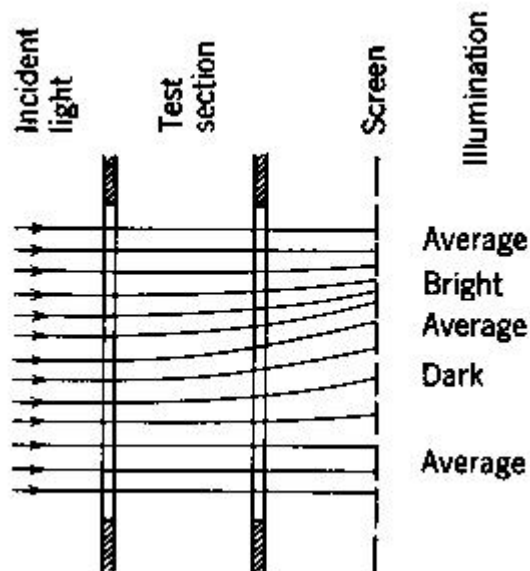


Fig. 2.8 The Shadowgraph effect [21]

The shadowgraph system used in this study is shown with the tunnel in Fig. 2.9, and schematically in Fig. 2.10. The light source, film, and all lenses were mounted on an optical rail to insure proper alignment. Light was produced by an argon spark-gap generator with a flash duration of approximately 1  $\mu$ sec. Two lenses were used to collimate the light before it passed through the test section, and a third provided magnification after the test section. Most photos were taken using 2.875 in. by 3.25 in. (7.3 cm by 8.26 cm) ISO 3000 Polaroid black and white film.

The film holder cover was kept open for the duration of a run, while the entire shadowgraph system and the tunnel were kept in a darkbox. A single triggering of the spark-gap provided the illumination to expose each shadowgraph image. Magnifications of up to 10x were possible with this system. In order to achieve the best possible clarity of the disrupting droplets, a magnification of 9.2x was used.

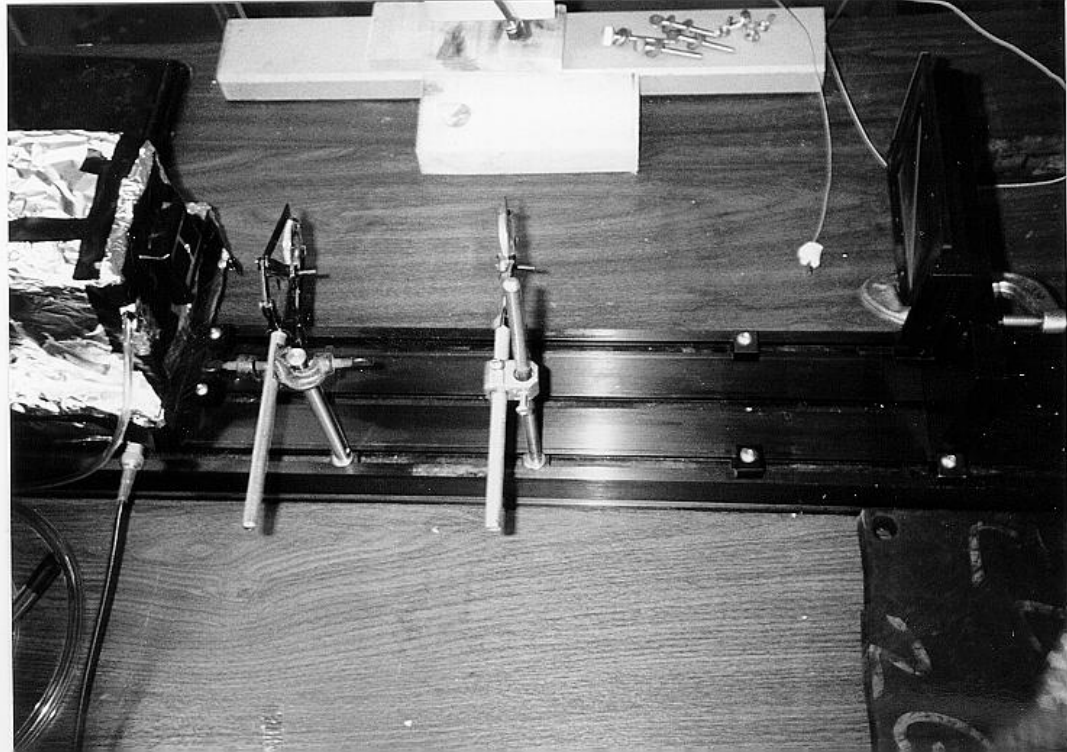


Fig. 2.9 The shadowgraph equipment used in the study. The spark gap generator is on the far left, the tunnel test section would be between the two lenses in the center. The black object in the upper right is the Polaroid film back.

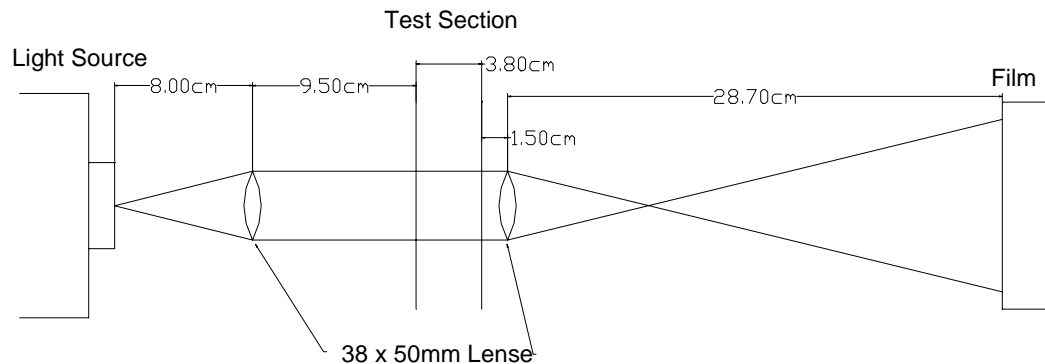


Fig. 2.10 Shadowgraph schematic

The shadowgraph technique with the above setup was used for both analyzing possible injection configurations, and for gathering the final data on droplet disruption.

Once developed, the shadowgraph Polaroids were digitally scanned into JPEG image format using an HP Scanjet II scanner. A 5x electronic magnification was applied during scanning in addition to the optical magnifications previously accomplished by the optical setup. The total magnification was therefore 46x. LViewPro Image enhancement software was used to increase image brightness and contrast. Magnifications were determined by photographing a narrow probe of known dimensions, and comparing the photographed dimensions (in pixels for the JPEG images) to the known values.

Large scale measurements of viewable image area, jet penetration, and shock angle were taken directly from the Polaroids using calipers. Drop positions were

measured from the scanned images. This was accomplished by reading the pixel position of the cursor at two or more positions. The length in pixels was calculated and converted into physical distance. Uncertainty in measured lengths using this method is estimated to be less than 0.01 mm. However uncertainty in droplet position can be as high as 0.1 mm because the point of injection is not always clearly visible in the photographs.

The shadowgraphs used in this study contained a large amount of 'noise' or background clutter, particularly at the high magnifications. In each photo such objects as: dirt on the lenses, residue on the tunnel windows, and out-of plane unfocused droplets created many specs and 'ghost droplets' which were difficult to differentiate from actual droplets. This made identification of droplets (especially those undergoing disruption) difficult in many of the photographs. Two methods were used to identify droplets. Potential droplets had to be significantly more distinct than the surrounding noise, and fall within a size window of 0.09 to 0.11 mm. Photographs containing objects which met these criteria were then checked against photographs taken immediately before or after the test (with no flow or droplet injection occurring in the tunnel). If the object was only found in the photograph of the actual run, it was determined to be a droplet.

Tunnel flow properties were calculated from the free-stream pressure measured from static pressure taps in the bottom of the test section. The taps are located 1.0, 5.0, 7.625, 10.5 and 14.0 in. (2.54, 12.70, 19.37, 26.67 and 35.56 cm) downstream of the tunnel entrance. The last three pressure taps are located in the test section, 0.15, 3.02 and 6.52 in. (0.37, 7.67 and 16.56 cm) downstream of the test section entrance. Static pressures were measured with a mercury monometer. Accuracy was limited primarily by

oscillations in the mercury column caused by the rapid changes in tunnel pressure. Due to the short duration of the typical run, these oscillations did not die out before measurements were taken. Therefore a typical inaccuracy of 0.5 in Hg was encountered in the pressure measurements.

## **2.5 Run Conditions**

Initial tunnel performance was calculated with a nozzle inserted into the hole in the top of the test section. The nozzle tapered to a 0.0625 in. (1.59 mm) exit orifice. The tunnel test section static pressure just upstream of the nozzle entrance was 0.174 atm. Using this value all of the other properties were calculated with isentropic relations. The measured Mach number based on the static pressure was 1.8, corresponding to a flow velocity of 482 m/s (1581 f/s). This pressure and velocity could be sustained for 15 seconds. The calculated nominal static temperature in the test section was 181 K. All of the data for the tunnel were measured and calculated upstream of any shocks which resulted from the flow entering from the nozzle in the top of the test section.

One additional factor which affects tunnel performance is humidity. The increased humidity of the air being drawn into the tunnel during the summer months (when most data was collected) caused significant occurrence of water condensation on the tunnel's internal metal surfaces just upstream of the throat. Condensation forming at these points was dragged downstream and across the quartz windows. In some runs this problem was severe enough to prevent the gathering of any useful data. In all cases, the interior surfaces of the quartz windows had to be cleaned prior to the start of the next run. The

condensation did not have any observable effect on static pressure in the tunnel free-stream. Some of the shadowgraphs shown in Chapter 4 show the marks of condensation on the pictures.

### **3. Simple Analysis of Droplet Injection**

#### **3.1 Concerns**

One of the earliest concerns about the success of producing liquid droplets in the WPI supersonic tunnel was the effectiveness of the injection technique. As originally designed, the tunnel was intended to allow droplets to be injected tangentially at the tunnel entrance. There were two primary concerns: First, that the droplet may have accelerated excessively, so that by the time it reached the test section the relative velocity between the droplet and the free-stream was no longer supersonic. The second concern was that the droplet might have already disrupted by the time it reached the test section. Either of these cases would prevent the generation of any meaningful data on droplet disruption and vaporization. Normal injection in the test section would potentially solve both of these problems. However, this form of injection substantially complicates the flow field around the droplet by adding a perpendicular component to its velocity and introducing a transverse jet structure. A secondary advantage is that the entire injection process would be observable. An idealized numerical model was developed and used to evaluate the relative effectiveness of tangential vs. normal injection.

#### **3.2 Simple Injection Model**

The critical quantity is the droplet velocity,  $V_D$ . This can be found by solving for the droplet acceleration. The following equation was used as the basis for the numerical model:

$$F_D = K_D \rho_A d_D V_{rel}^2 \quad (8)$$

where  $F_D$  is the force on the droplet,  $K_D$  the drag coefficient,  $\rho_A$  the density of the airflow,  $d_D$  the diameter of the droplet (assuming a spherical droplet), and  $V_{rel}$  the relative velocity between the droplet and the airflow ( $V - V_D$ ). From this expression, the acceleration of the droplet is:

$$a_D = \frac{F_D}{m_d} = \frac{K_D \rho_A d_D V_{rel}^2}{\rho_D V_D} \quad (9)$$

$$a_D = \left( \frac{K_D \rho_A d_D}{\rho_D V_D} \right) (V - V_D)^2 = \left( \frac{K_D \rho_A d_D}{\rho_D V_D} \right) \left( V - \frac{dx}{dt} \right)^2 \quad (10)$$

$$a_D = \left( \frac{\rho_A d_D}{\rho_D V_D} \right) K_D \left( V^2 - 2V \frac{dx}{dt} + \left( \frac{dx}{dt} \right)^2 \right) \quad (11)$$

Where  $\rho_D$  is the density of the droplet, and  $V_D$  the volume of the droplet.  $V_D = (dx/dt)$  is the velocity of the droplet, where  $x$  is the droplet position measured downstream from the tunnel entrance.  $K_D$  is not constant in the transonic range, but studies have shown that it is largely independent of droplet diameter for spherical droplets [22]. Using the data of Charters & Thomas [22], the following approximate functions were used for  $K_D$ :

$$M_{rel} < 0.5 : \quad K_D = 0.192 \quad (12)$$

$$M_{rel} \geq 0.5 : \quad K_D = 0.3198 + 0.2987(M_{rel} - 1) - 0.0809(M_{rel} - 1)^2 - 0.3606(M_{rel} - 1)^3$$

Using the equations derived above for the droplet acceleration, and the approximations given by Charters & Thomas, a general fourth order Runge-Kutta algorithm was used to approximate the droplet velocity as a function of position, for droplets injected both

normally in the test section and tangentially at the tunnel entrance. In these cases the droplet was assumed to have no velocity components perpendicular to the tunnel free-stream flow. Interactions between neighboring droplets were also ignored. All droplets were assumed to be sufficiently separated such that they did not affect each other.

### 3.3 Model Results

Two nondimensional quantities are used to determine if the droplet is within the range of acceptable conditions ( $V_D$  supersonic, droplet still undisrupted by aerodynamic forces). The first is the relative Mach number, which was calculated by the model using the velocities found by the Runge-Kutta algorithm. The second quantity is the Weber number, which relates the inertial forces to surface tension [6, 9]. The specific variables used to determine the Weber number in this study are:

$$We = \frac{\rho_A V_{rel}^2 d_D}{\sigma_l} \quad (13)$$

Where  $\sigma_l$  is the surface tension of the test liquid (water was used in the model) at ambient conditions. This equation also used the relative velocity found by the Runge-Kutta algorithm. It should be pointed out that the Weber number determines not only if a droplet will disrupt but how long it takes to disrupt as defined by the characteristic disruption time.

Fig. 3.1 shows relative Mach numbers for a range of droplet sizes injected normally in the test section. The effects of any secondary jet structure, as well as bow shocks, are not included in this analysis and will be discussed later. The graphs of Mach

number show only components in the direction of tunnel flow, therefore the droplet velocity is initially zero (in this direction). For the range of droplet sizes of interest in this study (0.1 to 0.5 mm, 0.0039 in. to 0.02 in.), the droplets will remain exposed to a relative Mach number greater than 1 for at least 0.03 m (1.18 in.). For Figs 3.1, 3.2, 3.3 and 3.4, the test section extends from 0.19 m to 0.37 m. This analysis does not address the issue of how to produce the droplet in the test section initially, only whether it will remain at a relative supersonic velocity for its observable duration.

Similarly, Fig. 3.2 shows the droplet relative Mach numbers for droplets injected tangentially at the tunnel entrance. For larger droplets, ( $D_0 > 0.5$  mm, 0.02 in.) this method still yields droplets traveling at supersonic relative velocities for the entire length of the test section. However smaller droplets ( $D_0 < 0.1$  mm, 0.0039 in.) will only experience supersonic velocities through the beginning of the test section (approximately 1 to 4 cm, 0.4 to 1.6 in.). In addition, even the larger droplets do not experience the high initial Mach numbers found in the test section injection method.

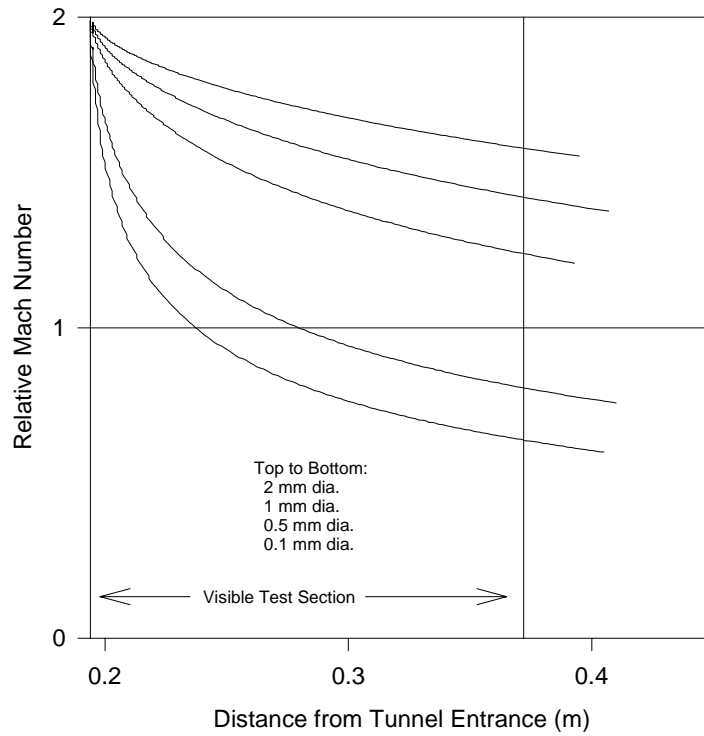


Fig. 3.1 Relative Mach number as a function of droplet size for normal injection in the test section.

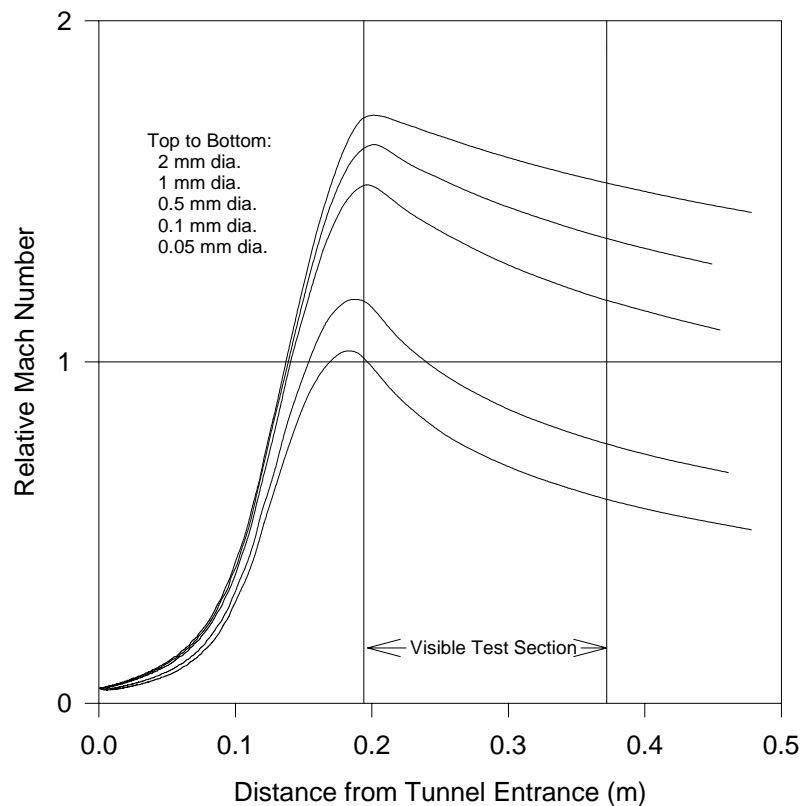


Fig. 3.2 Relative Mach number as a function of droplet size for tangential injection at the tunnel entrance.

Weber numbers were also calculated for the cases of injection at the tunnel entrance and in the test section. These are shown in Figs 3.3 and 3.4. Assuming a critical Weber number of the order of 100, Fig. 3.3 shows that droplets injected in the test section are already above the critical Weber number, except for very small droplet diameters. For injection at the tunnel entrance (Fig. 3.4) droplets also all exceed the critical Weber number. With a Weber number of 100, and the characteristic disruption time equations

given in Section 1, droplets under these conditions will disrupt after approximately 200  $\mu\text{sec}$ . Higher Weber numbers will disrupt after even shorter lengths of time. Since the droplets begin to disrupt when the Weber number exceeds the critical value, it is essential to have the droplets in the field of view of the diagnostic equipment when the critical value is exceeded. These results indicate that this is not possible using the tangential injection technique upstream of the test section. For the above reason, as well as the higher relative Mach numbers, injection in the test section was deemed necessary. This does not address the problem of how droplets can be injected tangentially without causing them to immediately disrupt.

Figs. 3.3. and 3.4 show calculations of Weber number neglecting, at this point, the effect of any shock in front of the droplet. Since this analysis did not model the actual injection process, the effect of the injection structure (including shocks) could not be taken into account. The no-shock case described by the model was taken as the maximum Weber number case, corresponding to the shortest disruption time. The minimum Weber number will occur behind a normal shock (which was neglected), since the presence of a shock will always decrease the Weber number. Since the minimum disruption time was the parameter of interest, all calculations were conducted for this analysis neglecting any shock effects.

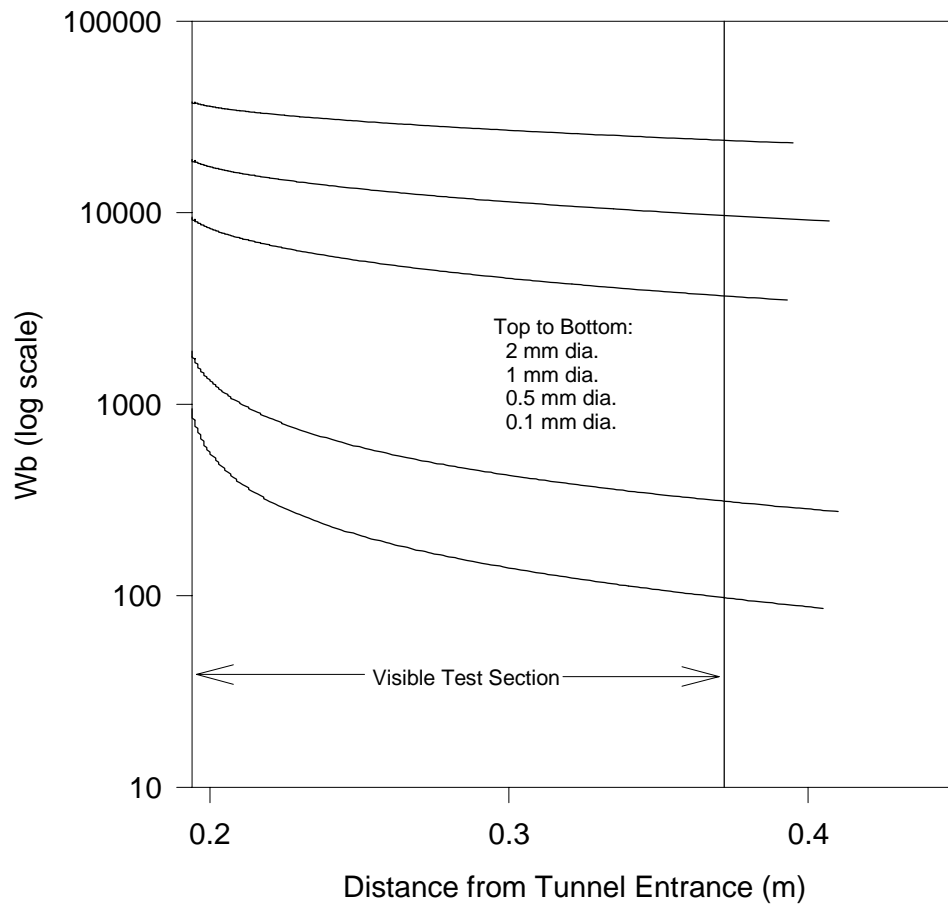


Fig. 3.3 Weber number for droplets injected normal to the tunnel flow in test section.

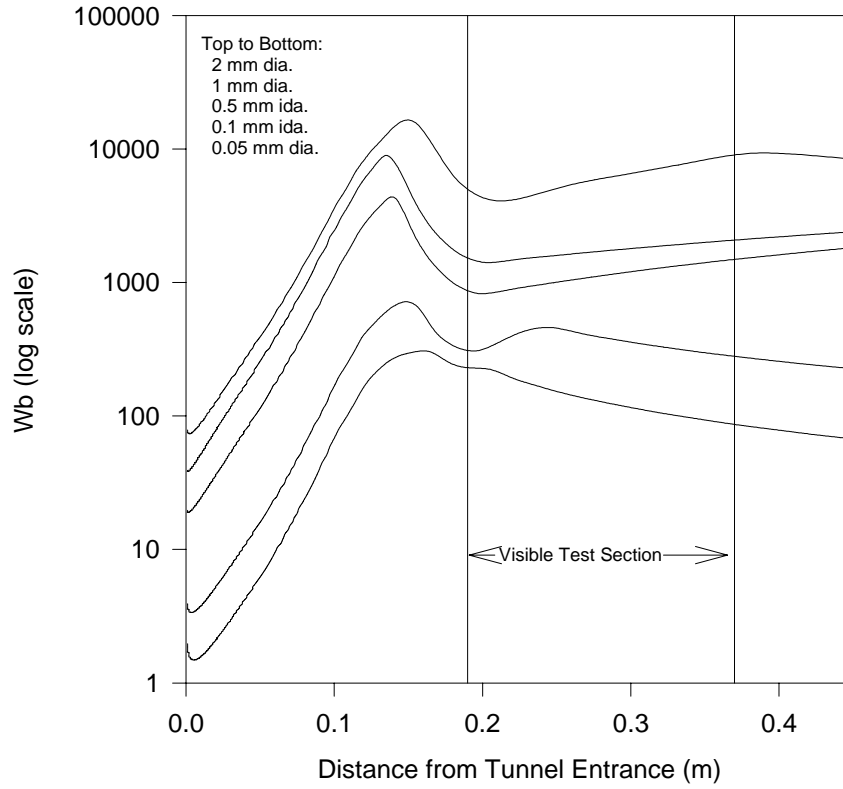


Fig. 3.4 Weber number for droplets injected tangentially at tunnel entrance.

The results gathered from the model for injection into the test section were also compared against the exact solution of equation 11 with constant free-stream velocities.

In this case the acceleration of the particle is:

$$a_D = \frac{C}{\left(Ct + \frac{I}{V}\right)^2} \quad (14)$$

where:

$$C = \frac{K_D \rho_A d_D^2}{\rho_D V_D} \quad (15)$$

The results obtained from these calculations matched those found by using the model. The previous section detailed the modifications that this injection scheme required, and their effect on tunnel performance. The actual code used is found in Appendix A.

### 3.4 Underexpanded Jet

The previous simplified analysis indicated that normal injection of droplets in the test section was necessary to insure droplet disruption in the test section. Chapter 2 describes the apparatus which was constructed to successfully accomplish the injection of droplets into the tunnel free-stream. This droplet injection procedure used a sonic cross flow injected perpendicularly to the tunnel free-stream flow. This transverse cross flow created an underexpanded jet structure, which greatly complicated the flow structure downstream of the injection point. The effect of this complicated structure was not taken into account in the simple model.

The prediction of the actual flow-field downstream of the injection point presented in the previous section is beyond the scope of this work. Numerous studies, both numerical [23, 24], and experimental [23, 25, 26], have attempted to model this problem. However few measurements or predictions have been carried out in the region near (within 5 jet diameters) the point of injection [23].

A simplified analysis was conducted to estimate the Weber number in the expansion region of the sonic jet, treating the flow-field as an underexpanded sonic jet

exiting into a stationary atmosphere with a back pressure equal to that found in the tunnel free-stream behind a  $46.6^\circ$  bow shock (0.3182 atm.). This analysis neglected the free-stream flow velocity. Mach numbers and pressures were calculated along the centerline using the method of characteristics [27].

The flow conditions at several points along the centerline of the first cell of the expansion structure (upstream of the mach disk in Fig. 3.5) are shown in Table 3.1. The position of the droplets relative to the expansion structure was determined from shadowgraphs of the droplets being injected. Since the droplets generally have left the observed expansion structure by the time they travel 1.2 mm (the average droplet left the jet structure after traveling only 0.25 mm due to its higher momentum compared to the air in the jet), the conditions were only calculated up to 1.66 mm.

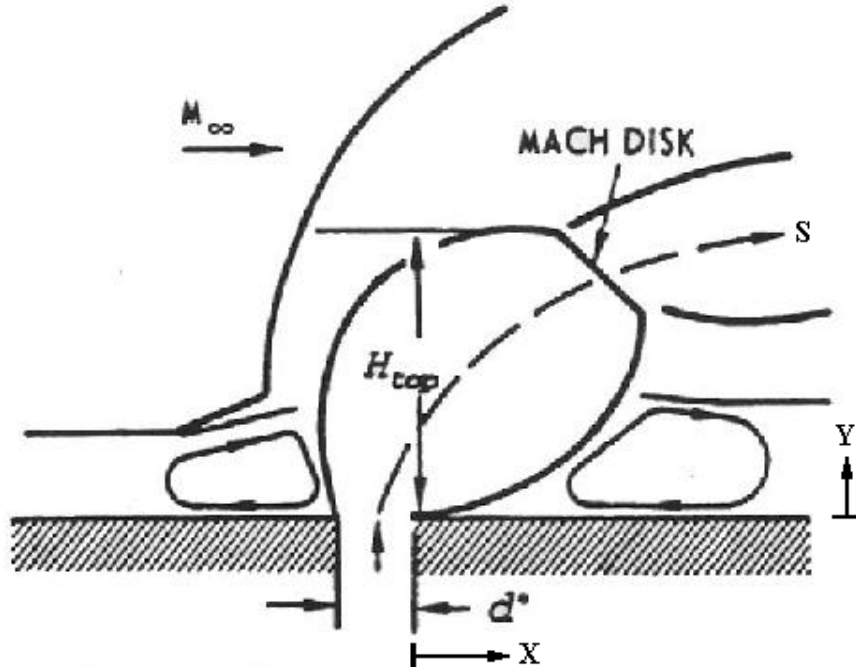


Fig. 3.5 Sonic jet structure [29]

Downstream Distance (mm)	T (K)	P (atm)	Flow M#	We
0.17	243	0.52	1.01	885.2
0.74	229	0.42	1.18	911.4
0.98	220	0.37	1.29	942.3
1.35	202	0.27	1.5	837.7
1.51	194	0.24	1.6	789.4
1.66	186	0.2	1.7	735.6

Table 3.1 Centerline flow-field conditions in the underexpanded jet. Weber numbers for a 0.1 mm diameter droplet.

Although the actual flow-field is more complicated than the analysis presented above, this analysis can be used to give a range of Weber numbers that can be expected in the actual flow-field. From this range of Weber numbers, the droplet disruption time can be predicted based on the maximum Weber number seen by the droplet as it passes through the injection structure and into the tunnel free-stream. The important results from this analysis are that the Weber number is not expected to change significantly through the expansion structure (less than 20%), and the magnitude of the Weber numbers to be encountered are similar to those found in the simple analysis shown in Fig. 3.3.

The initial conditions will be the most accurate using this analysis, with conditions further along the centerline diverging from this simplified solution as the actual flow-field deforms from the ideal underexpanded jet. The trend in conditions will be the same, decreasing temperature and pressure, and increasing Mach number as the downstream distance increases. The trend in Weber number is less straightforward, as it initially increases due to the increase in flow velocity, but soon reaches a peak value, after

which it decreases to a value below its initial value as the falling density begins to have a greater effect.

The initial and maximum Weber numbers (885.2 and 942.3) generated via this method were used to predict the disruption time of the droplet by aerodynamic forces only. The disruption time calculated for a droplet under the initial conditions is 1040  $\mu\text{s}$ , while the disruption time calculated for a droplet using the conditions at maximum Weber number (also the conditions at which all observed droplets have left the expansion field) is 1190  $\mu\text{s}$ .

## 4. Results

### 4.1 Sonic Jet Structure

The flow structure near the point of injection is characterized by three primary regions: the free-stream tunnel flow upstream of the shock ( $M_\infty$ ), the supersonic tunnel flow downstream of the shock, and the sonic jet entering the tunnel perpendicular to the free-stream flow. These regions are detailed in Fig. 3.5. Initially a normal shock, the bow shock upstream of the sonic jet changes to an oblique shock with an angle of  $46.6^\circ$ . Using this value, the flow conditions behind the shock were calculated using oblique shock relations.  $M_s = 1.375$ ,  $P_s = 0.3182$  atm.,  $T_s = 211$  K. Very near the point where the jet enters the free-stream, the bow shock is normal to the flowpath. Conditions in this region were calculated by treating the bow shock in this region as a normal shock.  $M_s = 0.6165$ ,  $P_s = 1.15$  atm.,  $T_s = 323.2$  K. Isentropic relations were used to calculate the conditions in the sonic jet at the entrance to the tunnel (beginning of the expansion structure). With  $M_j = 1.0$ ,  $P_j = 0.5283$  atm., and  $T_j = 243$  K.

Changes to the alignment of the optics, in order to increase sensitivity, revealed that different optical configurations were required for obtaining the best images of the bow shock, sonic jet structure, and liquid droplets. This precluded taking images that showed the jet structure and droplets at the same time (at the magnification required to observe the droplets, the bow shock is not within the field of view of the camera). Fig. 4.1 shows two examples of the bow shock and jet structure as the (unseen) liquid droplets are

being injected at ambient temperature. Fig. 4.2 shows the same features outlined for clarity.

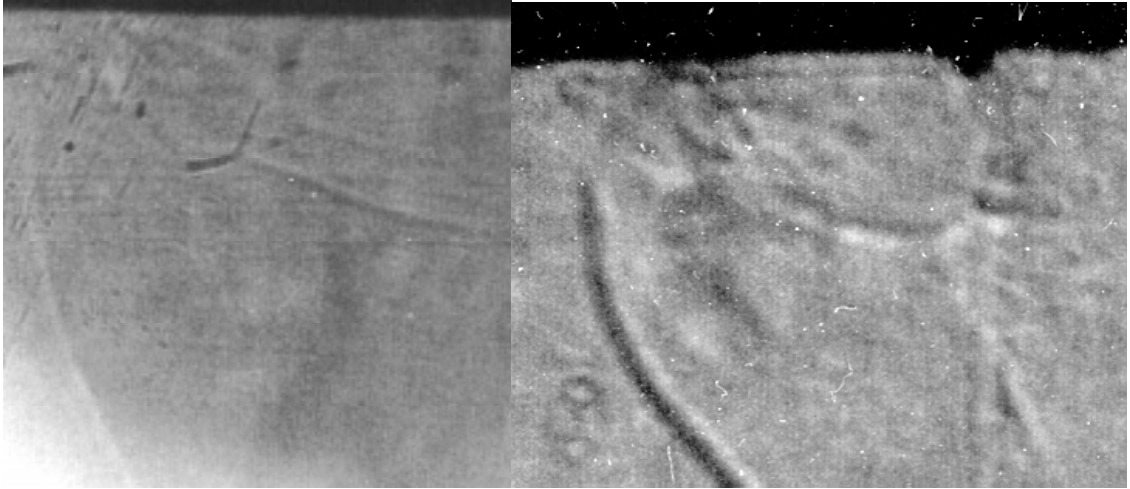


Fig. 4.1 Jet and shock structure, primary flow is from left to right, sonic jet enters from the top.

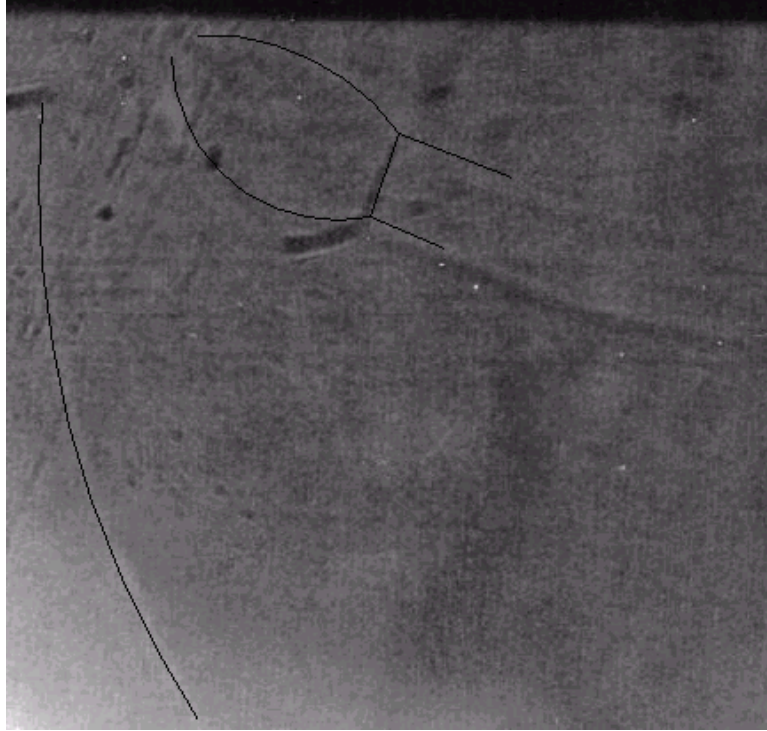


Fig. 4.2 Shock and jet structure outlined for clarity, primary flow is from left to right, sonic jet enters from top.

The penetration of a normal sonic jet into a supersonic flow has been correlated by Cohen et al. [28]:

$$\frac{H_{top}}{d^*} = 1.51 \left( \frac{(\rho V^2)_j}{(\rho V^2)_\infty} \right)^{0.5} \quad (16)$$

Where  $H_{top}$  is the penetration of the normal jet, measured from the tunnel wall to the top of the Mach disk of the sonic jet (as shown in Fig. 3.5). The effective orifice diameter,  $d^*$  is calculated by scaling the actual orifice diameter,  $d$  by the square root of an experimentally calculated discharge coefficient:

$$d^* = d \sqrt{C_D} \quad (17)$$

For a sharp-edged orifice such as that used in this study, the discharge coefficient will likely be in the range of 0.8 to 1.0, and the actual orifice diameter was 0.0625 in. (0.159 in.).

Using the above equation and the tunnel and nozzle properties previously calculated above and in Section 2, the predicted value for  $\frac{H_{top}}{d^*}$  was 0.0044. Measurement of the actual height of the Mach disk from the shadowgraph images shown in Fig. 4.2 produced a value of  $\frac{H_{top}}{d^*}$  of 0.002. However the equation from Cohen is for a jet exiting into an open flow. Other studies have shown that wall effects in a narrow tunnel can significantly reduce the penetration of the jet [29].

#### **4.2 Droplet Path**

Pictures were taken as discussed in section 3.1 for a range of droplet temperatures from ambient conditions (18° C) to 66° C. In each photo, typically between 5 and 30 ethanol droplets are visible at various positions and levels of disruption.

A composite graph was constructed using the first photo of the jet structure shown in Fig. 4.3, and the droplet positions shown on 11 different photographs that showed non-disrupting drops. The graph is shown in Fig. 4.3 and shows the range of droplet positions which define the area where droplets will be found. Also shown for comparison are the boundaries of the underexpanded jet structure.

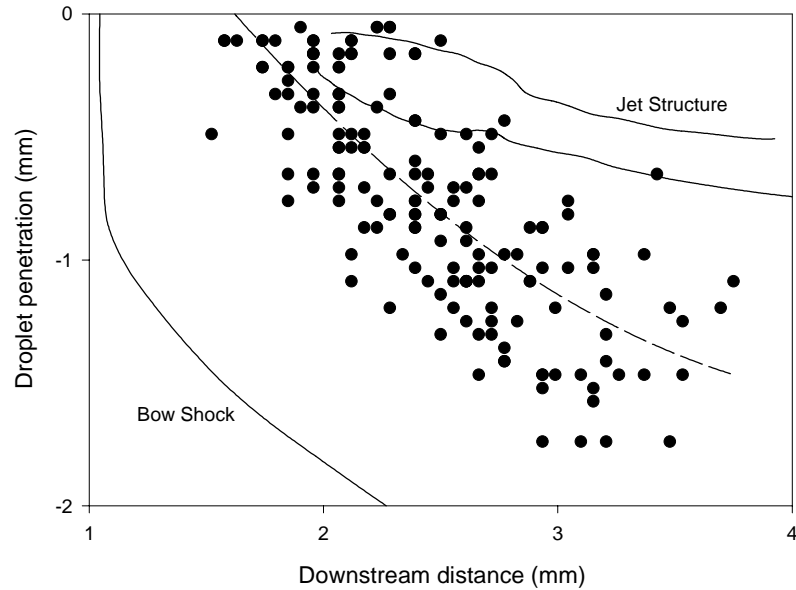


Fig 4.3 Composite graph of all droplets under non-disrupting conditions. Primary flow is from left to right. The dashed line indicates the average droplet path. Distance along the x-axis is measured from a common origin.

It can be seen from Fig. 4.3 that the droplets do not generally follow a path similar to that of the jet. This is not surprising, considering the higher density of ethanol relative to the surrounding air. The drops also have a much higher momentum (approximately 1500 times higher) than the surrounding air upon entering the tunnel. Therefore droplets will follow a path more perpendicular to the primary flow than the surrounding air, as they accelerate to the free-stream velocity.

The droplets in Fig. 4.3 show a large amount of scatter from the average droplet path marked by the dashed line. There are two primary reasons for this scatter. The first cause stems from the fact that the nozzle/needle assembly was removed from the tunnel between each run. A slight variation in needle position resulted from this practice. This small variance caused the droplet paths to vary between subsequent runs. Not noticeable in the individual photos, the composite graph of Fig. 4.3 clearly shows this scatter.

The second cause for the scatter seen in Fig. 4.3 is the scatter from the individual droplet paths which appear in each photo. As shown in the schematic in Fig. 2.5, the needle is held fixed only at the top, while most of its length remains free. The air entering horizontally just above the needle must be turned a full ninety degrees as it enters the nozzle. Although most of this turbulent structure is removed by the effect of the converging nozzle as the flow accelerates, it is speculated that slight vibratory modes induced at the top of the needle and magnified by the needle's length could exist. As a result the needle exit changes position as the droplets are being stripped off by the flow. The effect is pronounced enough so that in some individual photos, neighboring droplets seem to form oscillatory paths. Fig. 4.4 shows a typical photo of droplets being injected into the tunnel. In this photo a group of droplets in the upper left corner can be seen clumped together in a tight group. Such groups were not included in the results or discussion of this study. Only single, isolated drops and their behavior were studied.



Fig. 4.4 Typical photo of droplets (large dark circles) being injected into Mach 1.8 flow. Primary flow is from left to right, droplets being injected from upper left. Actual droplet size is approximately 0.09mm (0.0035 in.).

Fig. 4.3 also shows that the average droplet path leaves the observed jet structure after traveling approximately 0.25 mm (0.098 in.). The temperature and pressure on the centerline of the expansion structure calculated in Section 3 at a distance of 0.25 mm downstream of the point of injection is 240 K and 0.5 atm. (extrapolated from Table 3.1). The maximum distance any droplet was observed to travel before leaving the jet structure was 1.2 mm. At this distance along the centerline of the expansion structure, the temperature and the pressure were 210 K and 0.3 atm, respectively.

### 4.3 Droplet Disruption

Non-superheated droplets may suddenly become superheated by passing into a region where the local boiling point is below the droplet temperature. As the droplet travels from the nozzle exit plane, through the jet structure, and into the tunnel free-stream downstream of the bow shock, the local boiling point falls as the local pressure decreases. The level of superheat (if any) of the droplet correspondingly rises. It is assumed that there is negligible heat transfer between the droplet and the surrounding flow over the time period of interest (estimated to be approx. 5  $\mu$ sec).

Ethanol droplets were injected into the Mach 1.8 tunnel flow at a range of temperatures from 18° C to 66° C. Water was not used due to difficulties with freezing and icicle formation in the test section downstream of the injection site. Higher droplet temperatures would have caused the ethanol temperature in the line to exceed the boiling point (78.4° C at atmospheric pressure).

Boiling points for ethanol at the injection conditions were calculated from thermodynamic data for ethanol published in the Handbook of Chemistry and Physics [30]. At the nozzle exit plane, ethanol has a boiling point of 63° C, and a  $T_{SL}$  of 189° C. In the tunnel free-stream flow (downstream of the shock) the boiling point is 48° C, and the  $T_{SL}$  is 188° C. Using the analysis of Chapter 3, it was predicted that the droplets in the expansion structure do not experience pressures or temperatures below those encountered in the tunnel free-stream. Therefore the boiling point of a droplet in the injection structure was predicted to range between 48° C and 63° C. It should be noted that no attempts were made to produce droplets with temperatures near the superheat

limit at any point for reasons explained above. Table 4.1 shows the number of droplets which were produced in each of the three cases.

	<b>Liquid Temperature</b>	<b>Superheat Condition</b>
<b>Case I</b>	18 to 47° C	Droplet not superheated at any points
<b>Case II</b>	48 to 62° C	Droplet superheated only in tunnel free-stream
<b>Case III</b>	63 to 66° C	Droplet superheated at all points in tunnel (including jet structure)

Table 4.1 Superheat conditions

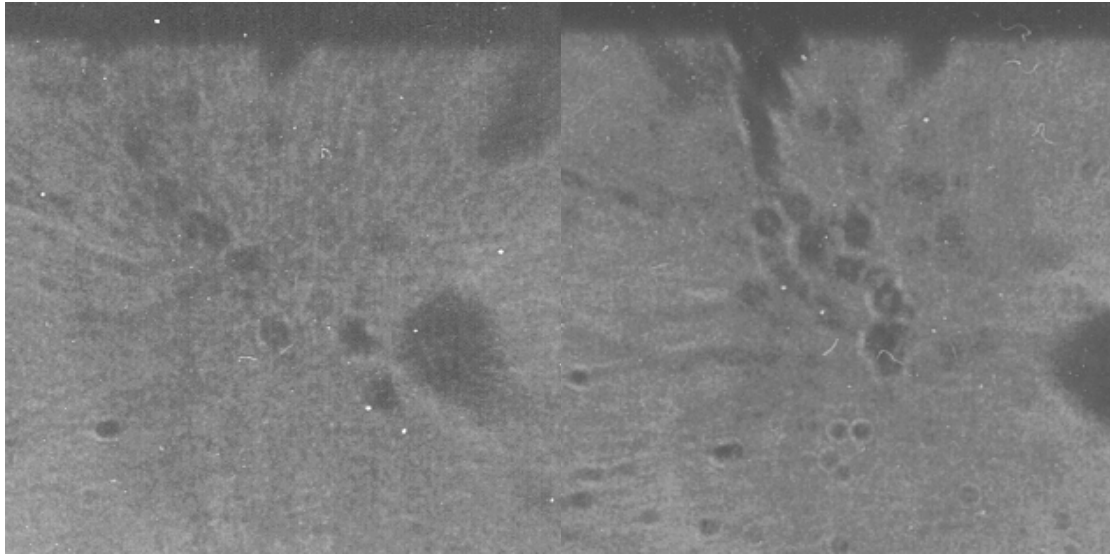
Drops in all temperature ranges did not pass through the bow shock, and there was no photographic indication of any shock structure directly in front of the drop. No drop at any point passed through a shockwave or Mach disk. Therefore only aerodynamic disruption processes were expected for a non-superheated drop.

The maximum Weber number for all droplets injected was seen immediately after injection into the free-stream. At this point the droplet was behind the normal section of the bow shock (though within the expanding jet flow) and was exposed to a relative horizontal velocity equal to the free-stream velocity behind the shock (206 m/s, 676 f/s). The Weber number seen for a 0.1mm (0.0039 in.) drop at this point was 738, well above the critical values found in previous studies.

Using the above Weber number the time for disruption can be calculated from the equations presented in Chapter 1. The predicted disruption time for the same 0.1mm (0.0039 in.) droplet was 130  $\mu$ sec. The relation found by Tan & Bankoff [10] assumed a

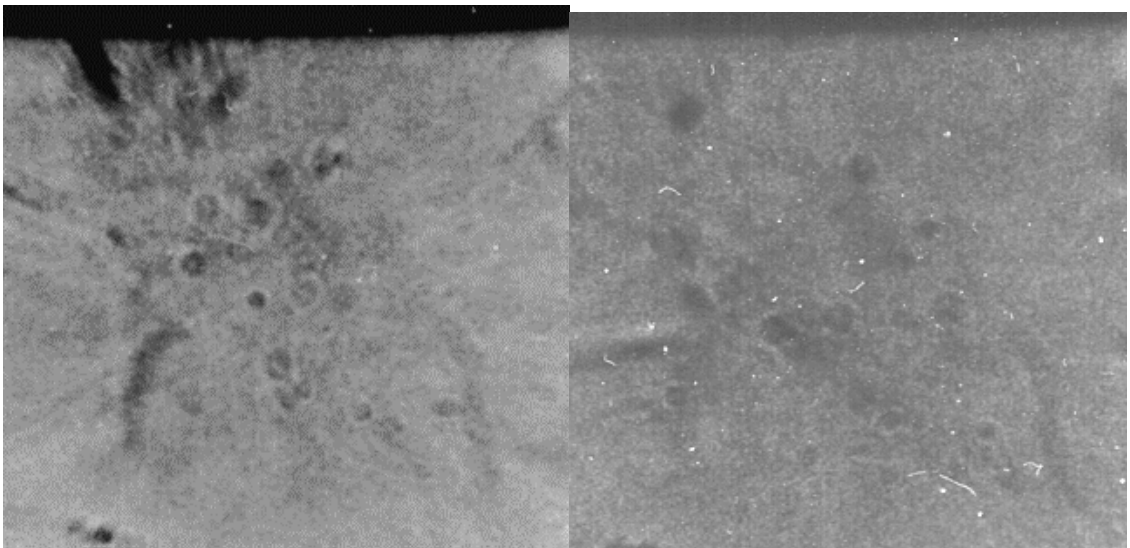
steady flow. In the cases seen in this study, the droplet moved through the jet structure, changing both the Weber number (which would happen even in a steady flow as the droplet accelerates) and the density ratio. However, the disruption time calculated by assuming a constant density ratio, was over 15 times greater than the time for which the droplets were observed in this study (8  $\mu$ sec, estimated based on the size of the observable region and the droplet perpendicular velocity). Therefore it was assumed that no disruption due to aerodynamic effects were observed (In Section 3 higher Weber numbers were calculated within the sonic jet, however the disruption times were shorter due to the lower relative velocities encountered).

For droplets for Case I, no definite signs of disruption were noted. Although some photos showed possible signs of disruption near the edge of the observable range, their proximity to the edge of the photo made it difficult to accurately determine whether they were disrupting drops or simply a result of edge distortion caused by the optics. These possible disruptions were therefore not recorded as disruptions in this study. All recorded disruptions were required to be well within the observable range and to be clearly unambiguous. Examples of photos taken of droplets for this case appear in Fig. 4.5.



a)

b)

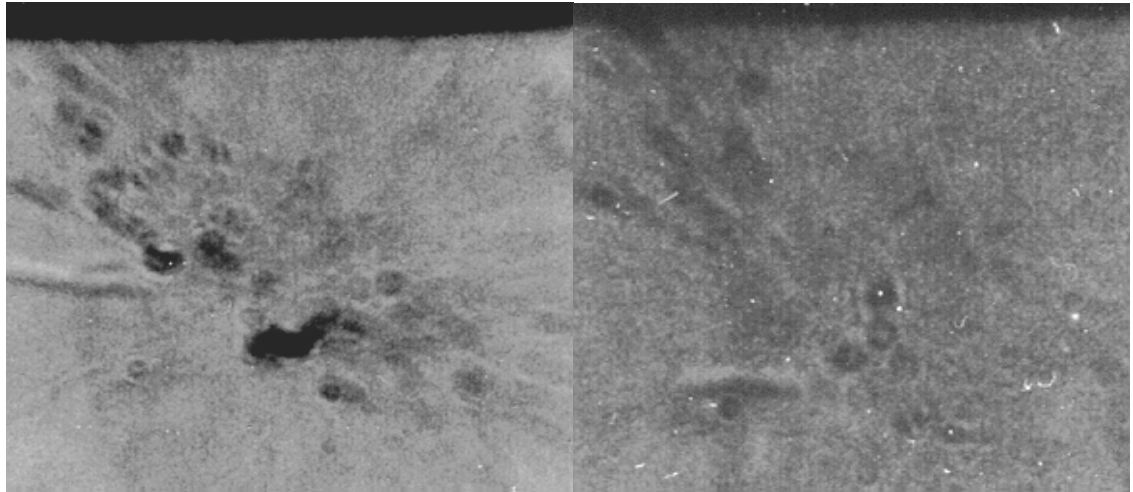


b)

d)

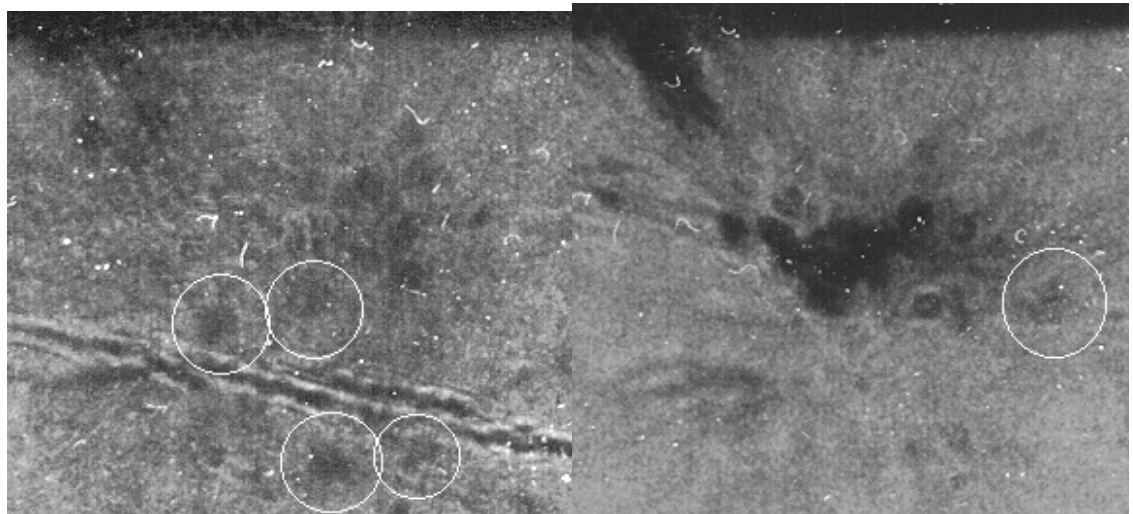
Fig. 4.5 Non disrupting droplets injected into a Mach 1.8 flow. Primary flow is from left to right, droplets injected from upper left. a)  $T_D = 18^\circ \text{C}$ , b)  $T_D = 29^\circ \text{C}$ , c)  $T_D = 39^\circ \text{C}$ , d)  $T_D = 46^\circ \text{C}$ .

The droplets for Case II (48 to 62° C) became superheated once they passed out of the jet structure. However as mentioned before, it was difficult to take clear photos showing both the droplets and the jet structure. The determination of whether a droplet was in or out of the jet structure (considered to be within the visible boundaries of the expansion region) was accomplished by comparison between images of the injected droplets, and the measured position of the jet structure. This is reinforced by the typical jet structure shown in Fig. 4.4 which shows most droplets leaving the jet structure at a penetration depth of 0.25 to 0.5 mm (0.0098 to 0.02 in.). All of the disrupting droplets identified in this range were found at greater depths than those for Case III, where the droplets were superheated immediately upon injection. Fig. 4.6 shows photos of droplets being injected in this range.



a)

b)



c)

d)

Fig. 4.6 a)  $T_D = 50^\circ \text{C}$  and b)  $T_D = 52^\circ \text{C}$  nondisrupting drops being injected into the Mach 1.8 flow. c)  $T_D = 56^\circ \text{C}$  and d)  $T_D = 62^\circ \text{C}$  show disrupting droplets (white circles). The dark horizontal lines are caused by condensation on the tunnel walls. Primary flow is from left to right, the droplets are injected from the upper left.

Although all droplets outside of the jet structure for Case II were superheated, signs of disruption were only seen for measured droplet temperatures greater than 54° C. Disruption was shown by two methods in this range. In the first method, single droplets appear larger and less strongly defined than those injected at lower/no levels of superheat. This agrees qualitatively with results from other studies of droplets disrupting in a chaotic or violent mode [10, 14, 31]. In the second method droplets maintain their size and distinctness, but are seen to be surrounded by what might be a cloud of vapor, mostly downstream of the droplet. This corresponds to studies identifying a stripping mode of droplet disruption. The stripping mode of disruption appears to occur earlier than the chaotic mode, as shown in Fig. 4.5 d).

The sequence of disruption seen for Case II, that is: no disruption, followed by stripping and/or chaotic disruption, could be caused by the pressure drop through the expansion of the sonic jet. As the pressure quickly decreases (based on the estimated size of the expansion region and droplet velocity, the droplet passes through the jet structure in less than 3  $\mu$ sec) over a transition range, the droplet begins to boil at the point where the pressure is lowest (sides of the drop). The vapor being ejected from the droplet surrounds the drop contributing to the larger blurred appearance of the drop. As the pressure decreases further, the droplet becomes increasingly superheated and violently disrupts. Additional evidence of this process is seen in the droplets for Case III. This process is shown graphically in Fig. 4.7.

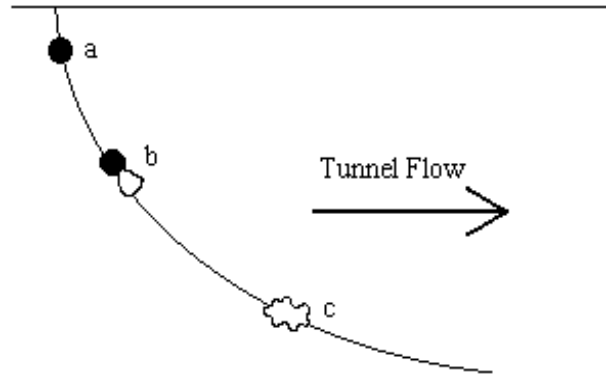
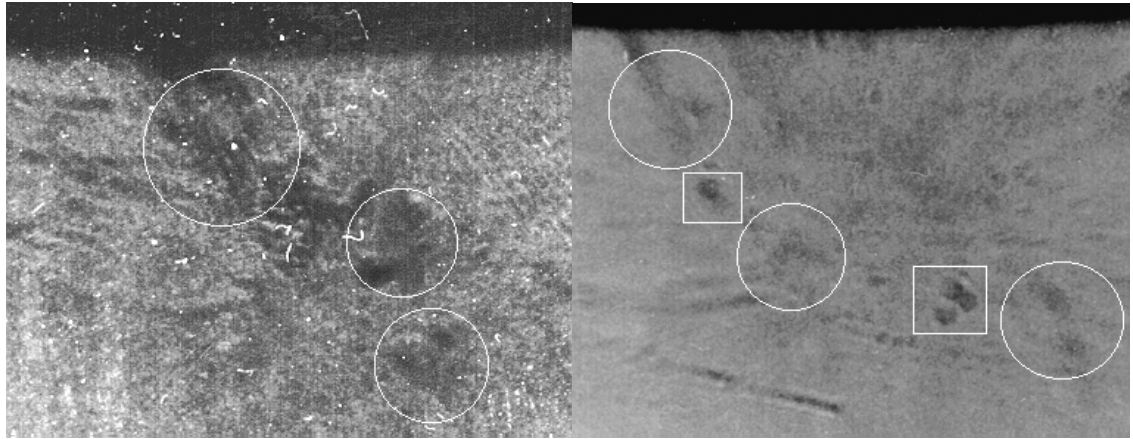


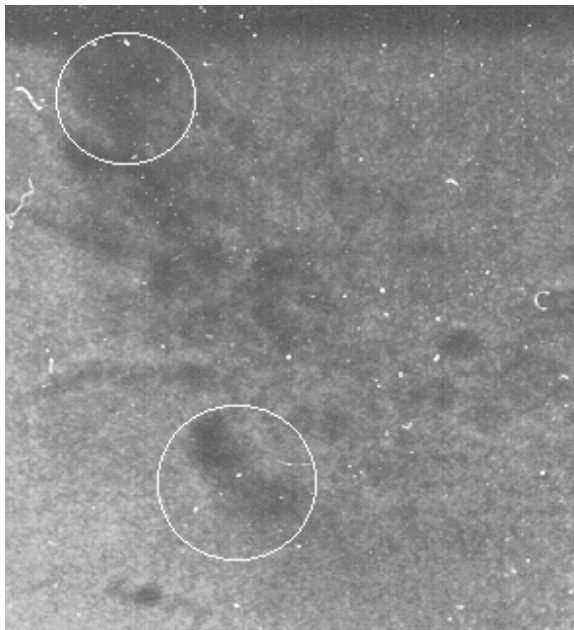
Fig. 4.7 A droplet at or just above the free-stream boiling point (low level of superheat) is injected as a stable droplet in the jet structure, a), as it penetrates deeper into the tunnel, the pressure falls as the droplet passes through the jet structure, b). At this point the droplet is slightly superheated, where the local pressure is lowest (the lee side), and begins to boil there. By the time the droplet has penetrated fully into the still lower pressure tunnel flow, c), it has fully disrupted.

In principle, droplets for Case III are superheated everywhere in the tunnel. However, the photos of droplets under these conditions in Fig. 4.8 clearly show some droplets traveling almost to the edge of the observable range while remaining in a nondisrupted state. Examples of these drops are marked with the white squares in Fig. 4.8 b). The most likely explanation is non-uniform heating in the ethanol supply or irregular cooling in the supply line and needle. Either could cause some of the droplets to be at a temperature slightly lower than the measured value (due to the proximity to the boiling point, it is not possible for the temperature to be significantly higher than the measured value). Even a small variation in temperature could cause droplets to be non-superheated due to the low levels of superheat used in this study.



a)

b)



c)

Fig. 4.8 a)  $T_D = 64^\circ \text{C}$ , b)  $T_D = 64^\circ \text{C}$ , c)  $T_D = 66^\circ \text{C}$ . White circles mark disrupting droplets, and squares mark non-disrupting drops.

All of the photographs in Fig. 4.8 show signs of droplet disruption in the chaotic mode, starting almost immediately after injection. Droplets at these positions are still

within the jet structure, and seem to be disrupting despite the fact that they are only slightly superheated (less than 5° C above the boiling point).

One of the drops in Fig. 4.8 b) deserves particular mention. The uppermost droplet marked in a white square appears to show a vapor plume emanating from its downwind side. The actual point of initiation of the vapor cloud is impossible to determine, as it is quickly blown downstream of the droplet by the free-stream flow, but it is assumed that the droplet would disrupt first on the sides, where the pressure is lowest. It is most likely that this pressure drop is in the free-stream region (outside of the jet, but still behind the bow shock), and therefore should be significantly (16° C) above the local boiling point. As mentioned above, it is possible that some of the droplets in this image, including the droplet in question, were at temperatures below the measured value. This would explain why this droplet is only boiling from the sides, while earlier droplets are disrupting in the chaotic mode.

Figs 4.9 through 4.11 show plots of the last observed non-disrupted drop and the first observed disrupting drop (if any) in each photo for all three cases (I, II and III). “First” and “last” here refer to distance traveled by the drop from the point of injection. However this distance can be defined in one of several different ways. Fig. 4.9 shows the downstream distance ( $x$ ) the drops in question have traveled, while Fig. 4.10 and Fig. 4.11 show the path-length ( $s$ ) traveled and penetration distance ( $y$ ) respectively. Path-length is the estimated total distance the drop has traveled, based on the positions of other drops in the photo. Penetration is simply the vertical distance the drop has fallen. Both penetration

and downstream distances were measured directly from the shadowgraph photos. Each of these figures were generated using all images from each temperature range.

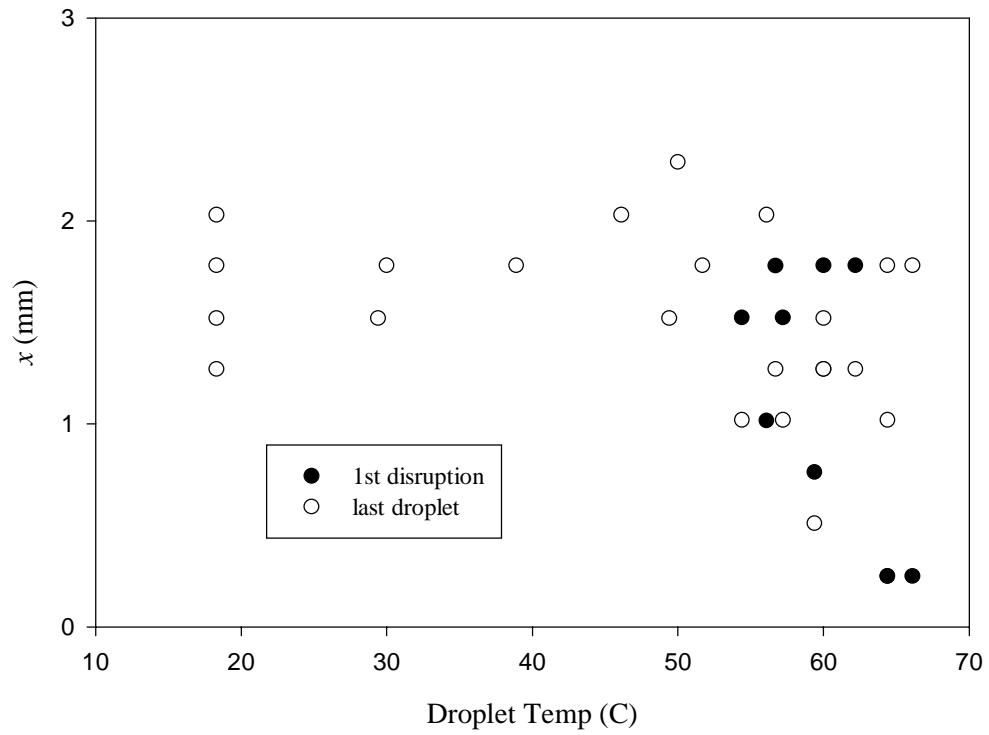


Fig. 4.9 First disruption (if any) and last undisturbed droplet downstream distance.

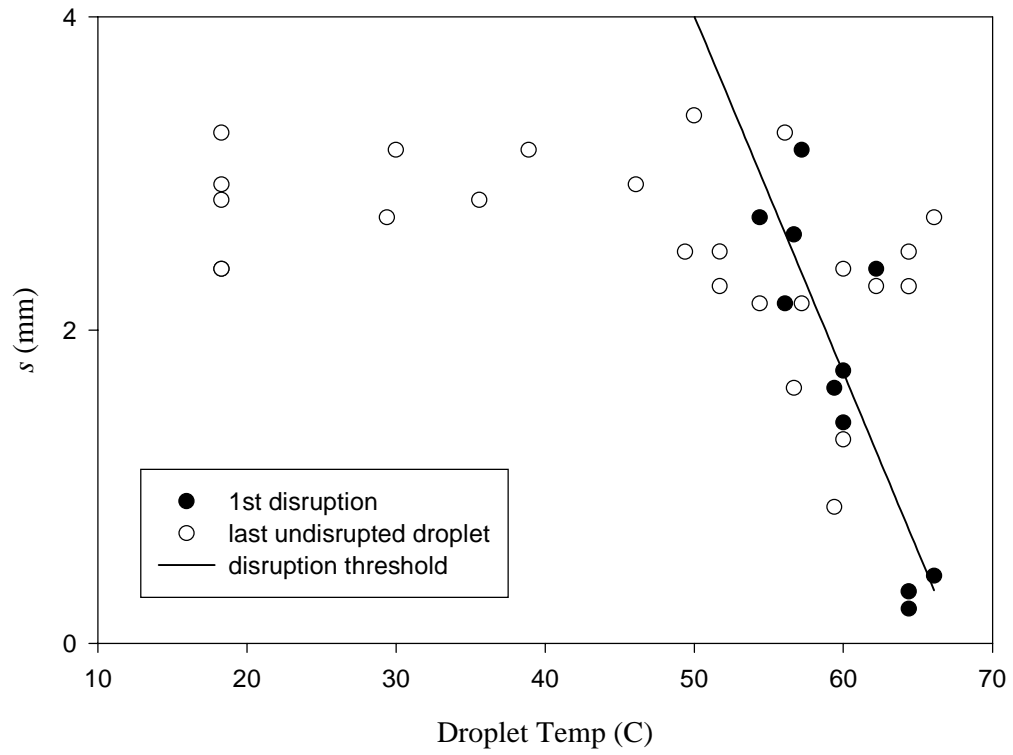


Fig. 4.10 First disruption (if any) and last undisrupted droplet total distance.

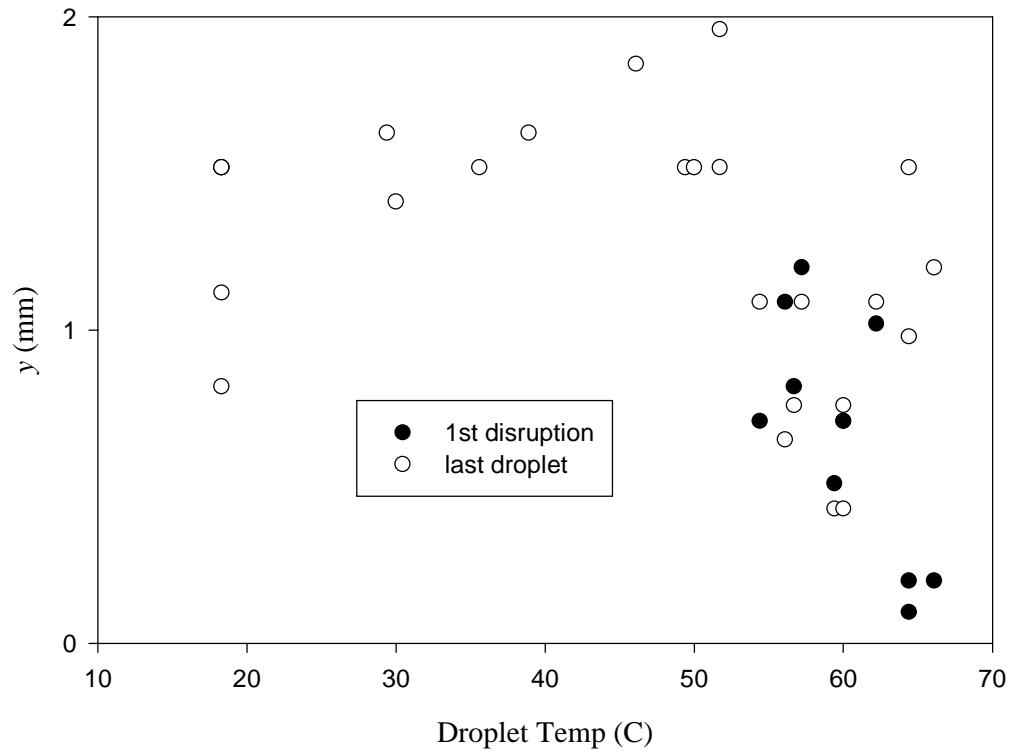


Fig. 4.11 First disruption (if any) and last undisrupted droplet penetration.

All three of the above figures (4.9, 4.10 and 4.11), show similar trends. Initially, droplets are only observed in a non-disrupted state and the last observed droplet appears at, or near, the edge of the observable field of view. It is expected that the actual distance to last undisrupted droplet may be much greater. As the temperature is increased, two events occur. First the distance to last non-disrupted droplet begins to fall, eventually disappearing. At the same time, disrupted droplets begin to appear, also starting near the

edge of the observable range and moving to near the point of injection as the temperature is increased. Since the data presentation of Fig. 4.10 appears to show the least scatter, that presentation of the data will be used in the following discussion. From this figure, disruption begins at a temperature of 54° C, and a path distance of approximately 3 mm (0.12 in.). The path distance for first occurrence of disruption drops sharply to less than 0.5 mm (0.02 in.) at 66° C. Through the same range, the last observed droplet's path fell from an average value around 3 mm to 2.5 mm (0.12 in. to 0.01 in.), with several points much lower.

The 1st disruption points of Fig. 4.10 were used to generate a linear fit labeled 'Disruption Threshold'. To the left of this line, undisrupted droplets are to be expected. To the right of the line, only disrupting droplets are expected. Mathematically:

$$s = 15.397mm - 0.2278 \text{ mm}/^{\circ}\text{C} * T_D \quad (18)$$

Where  $s$  is the path length (in mm) after which a droplet with a given temperature,  $T_D$  (in °C) would be expected to disrupt.

As was identified in previous discussion, some of the nondisrupting droplets recorded at the higher temperatures might have been at lower temperatures. This temperature variation may be partly responsible for the difference between the last observed droplet and first disruption distances for droplets at the same temperature. The undisrupted drops seen in the upper right of Fig. 4.10 can be explained this way. The other reason for this difference is the sparseness of droplets seen in some pictures. The first disrupted droplet may be observed some distance downstream of where it began to

disrupt, thereby showing a greater distance than the true disruption distance. A similar effect can occur with the last non-disrupting droplet.

## 5. Summary

The purpose of this study was to first demonstrate the ability to aerodynamically generate liquid droplets and inject them into a Mach 1.8 flow, and secondly, to observe the effect of low levels of superheat on the disruption rates of these liquid droplets.

Injection techniques involving tangential and normal injection were evaluated via calculations and a simple model. Both tangential injection at the tunnel entrance and normal injection at the start of the test section would have generated droplets experiencing supersonic relative velocities in the test section. However, the analysis indicated that injection at the tunnel entrance would produce droplets which would exceed the critical Weber number, and possibly disrupt before they progressed to the test section. Only injection in the test section insured that the entire disruption process would be observed, and this method was selected for this work.

An existing supersonic tunnel was modified to allow normal injection in the test section. Droplets were aerodynamically generated in a converging nozzle and successfully injected into the Mach 1.8 flow. The injection technique generated droplets by shearing drops of heated liquid ethanol from the end of a needle inserted upstream of the throat of the converging nozzle. After being sheared from the needle, the liquid drops were accelerated into the tunnel test section free-stream before leaving the jet structure. The droplets generated were of a consistent and repeatable size and frequency sufficient for the study. Droplets were injected at a range of temperatures from ambient to 66°C, which ranged from nonsuperheated to low levels of superheat under tunnel conditions behind

the bow shock. The shadowgraph method was used to determine the position at which droplets disrupted.

Nonsuperheated liquid ethanol droplets did not disrupt over the time span which they were observed. At low levels of superheat the droplets were shown to disrupt over the same time span. The observed disruption times were much shorter than those predicted for aerodynamic disruption alone. Droplets disrupted in the free-stream (behind the bow shock) for all temperatures above the boiling point. At higher temperatures the droplets also disrupted in the jet structure. Through transition temperatures, droplets began to boil first, shedding a fine mist that appeared on the downstream side of the droplet, before continuing to disrupt in the chaotic mode. The observed disruption modes matched those predicted by previous studies for droplets in a similar Weber number range. The presence of both disrupted and non-disrupted droplets in the same area of the flow at the same average temperatures indicated the presence of nonuniform droplet heating. Droplets at high levels of superheat could not be generated by the facility used for this study.

The main results of this work are summarized as follows:

- Normal injection is preferred over tangential injection.
- An aerodynamic droplet generator can be used to inject liquid droplets into a supersonic flow, without causing premature disruption.
- Ethanol droplets quickly disrupt in a Mach 1.8 air flow at low levels (1 to 28 °C) of superheat, while nonsuperheated droplets under the same conditions do not disrupt as quickly.

- The droplets appeared to disrupt in chaotic and stripping modes, consistent with the high Weber numbers involved.
- The 0.1 mm droplets used in this study typically disrupted after traveling 0.25 to 2.0 mm. The disruption time for the 0.1 mm (0.0039 in.) diameter droplets was approximately 2 to 4  $\mu$ sec (estimated from droplet penetration and initial velocity) for a level of superheat of 1 to 28° C.
- The momentum difference between the ethanol droplets and the air of the sonic jet caused injected drops to pass outside of the jet structure. Injected droplets passed out of the jet structure after traveling approximately 0.25 mm (2  $\mu$ sec after injection, estimated).

Several recommendations for further work can be made. One of the most important is the use of a diagnostic system with greater resolution than that used in this study. A shadowgraph system with greater magnification would more accurately record the level and mode of disruption of individual droplets, as well as provide greater detail of the expansion jet structure. Also a system that allows the testing of liquids at higher levels of superheat would be required to add data in that area.

In addition there are several improvements that can be made to the experimental system to increase the quality of the data which is generated. Heating of the tunnel walls or control of the atmospheric humidity could be used to reduce or remove the condensation problem which degraded the quality of the shadowgraphs. The suspected needle vibration could be removed to create a more repeatable and predictable droplet

path.

## REFERENCES

1. Kay, I.W., Peshke, W. T., and Guile, R. N., "Hydrocarbon-Fueled Scramjet Combustor Investigation," *Journal of Propulsion and Power*, March-April, 1992.
2. Alexander, D. R., and Armstrong, J. G., "Explosive vaporization of aerosol drops under irradiation by a CO<sub>2</sub> laser beam", *Applied Optics*, Vol. 26, No. 3 February 1, 1997.
3. Hermanson, J. C., "Disruption and Vaporization of Superheated Droplets in Compressible Flow", *National Science Foundation Proposal 9733830*, July 1997.
5. Patel, P. D., and Theofanous, T. G., "Hydrodynamic Fragmentation of Drops", *Journal of Fluid Mechanics*, Vol. 103, 1981.
4. Jacobs, J. W., Jenkins, D. G., Klein, D. L., and Benjamin, R. F., "Nonlinear growth of the shock-accelerated instability of a thin fluid layer," *Journal of Fluid Mechanics*, 1995.
6. Frost, D. L., "Initiation of explosive boiling of a droplet with a shock wave", *Experiments in Fluids*, May, 1989.
7. Hirahara, H., and Kawahashi, M., "Experimental investigation of viscous effects upon a breakup of droplets in high-speed air flow," *Experiments in Fluids*, Vol. 13, 1992.
8. Engle, O. G., "Fragmentation of Waterdrops in the Zone Behind an Air Shock", *Journal of Research of the National Bureau of Standards*, Vol. 60, No. 3 March 1958.
9. Reichman, J. M., and Temkin, S., "A Study of the Deformation and

- Breakup of Accelerating Water Droplets”, *Proc. Int. Coll. on Drops and Bubbles*, Pasadena, CA, 28-30 August 1984 .
10. Tan, M. J., and Bankoff, S. G., “On the Fragmentation of Drops”, *Journal of Fluids Engineering*, Vol. 108, March 1986.
  11. Reid, R. C., “Superheated Liquids”, *American Scientist*, Vol. 64, March-April 1976.
  12. Moore, G. R., "Vaporization of superheated drops in liquids," Ph.D. thesis, Univ. of Wisconsin, Madison, Wis, 1956.
  13. Wakeshima, H., and Takata, K., "On the limit of superheat," *Journal of Phys. Soc. (Japan)*, Vol 13.
  14. Frost, D., and Sturtevant, B., “Effects of Ambient Pressure on the Instability of a Liquid Boiling Explosively at the Superheat Limit”, *Transactions of the ASME*, Vol. 108, May 1986.
  15. Dabora, E. K., “Laser Ignition of Liquid Fuel Drops”, Combustion in Reactive Systems, Progress in Astronautics and Aeronautics, Princeton Combustion Research Laboratories, Inc., Princeton, New Jersey, Vol. 76, 1979.
  16. Kafalas, P., and Hermann, J., “Dynamics and Energetics of the Explosive Vaporization of Fog Droplets by a 10.6- $\mu\text{m}$  Laser Pulse”, *Applied Optics*, Vol. 12, No. 4, April 1973.
  17. Xie, J. G., Ruekgauer, T. E., Armstrong, R. L., and Pinnick, R. G., “Evaporative Instability in Pulsed Laser-Heated Droplets”, *Physical Review Letters*, Vol. 66, Number 23, June 10, 1991.

18. Beltran, J. M., Chris, B., and Vickers, S. M., "Oil Droplet Injection Into Compressible Flow", Major Qualifying Project, Worcester Polytechnic Institute, January 1997.
19. Green, G. J., Takahashi, F., Walsh, D. E., and Dryer, F. L., "Aerodynamic Device for Generating Mono-disperse Fuel Droplets", *Combustion Institute Eastern Section Technical Meeting*, Clearwater Beach, FL, December 1988.
20. Rohsenow, W. M., and Hartnett, J. P., *Handbook of Heat Transfer*, McGraw-Hill Book Company, New York, 1973.
21. Liepmann, H. W., and Roshko, A., *Elements of Gasdynamics*, John Wiley & Sons, Inc., New York, 1957.
22. Charters, A. C., and Thomas, R. N., "The Aerodynamic Performance of Small Spheres from Subsonic to High Supersonic Velocities," *Journal of the Aeronautical Sciences*, October, 1945.
23. Margason, R. J., "Fifty years of jet in cross flow research", *AGARD, Computational and Experimental Assessment of Jets in Cross Flow*, Nov. 1993.
24. Harloff, G. J., and Lytle, J. K., "Three-dimensional viscous flow computations of a circular jet in subsonic and supersonic cross flow", NASA Technical Report NASA-CR-182153, Sverdrup Technology, Inc., Jul., 1988.
25. Kraemer, G. O., and Tiwari, S. N., "Interaction of two-dimensional transverse jet with a supersonic mainstream", NASA Technical Report NASA-CR-175446, Old Dominion Univ., Dec., 1983.
26. Papamoschou, D., Sirignano, W. A., and Samuelsen, G. S., "Transverse injection of

liquid and gaseous fuels into subsonic/supersonic flow", NASA Technical Report AD-A2559771, California Univ., May, 1992.

27. Thompson, P. A., *Compressible-fluid Dynamics*, McGraw-Hill Book Company, New York, 1972.
28. Cohen, L. S., Coulter, L. J., and Egan, W. J., "Penetration and Mixing of Multiple Gas Jets Subjected to a Cross Flow," *AIAA Journal*, Vol. 9, No. 4, 1971.
29. Hermanson, J. C., and Winter, M. "Mie Scattering Imaging of a Transverse, Sonic Jet in Supersonic Flow, *AIAA Journal*, Vol. 31, No. 1, January 1993.
30. *CRC Handbook of Chemistry and Physics*, CRC Press, Cleveland, Ohio, 79th Ed. 1998.
31. McCann, H., Clarke, L. J., and Masters, A. P., "An experimental study of vapour growth at the superheat limit temperature", *Journal of Heat and Mass Transfer*, Vol. 32, No. 6, 1989.

## Appendix A: Numerical Code for Droplet Injection

```

program premodel
c  droplet injected anywhere, variable properties

real x1, x2
real vstart(2)
integer nstep, nvar

nvar = 2
x1= 0
x2= 0.036

nstep= 200
vstart(1) = 0.001
vstart(2) = 0.0
c  write(*,*) '      x          y(1)          y(2)          dxdy(1)
dxdy(2) '
c  open(unit=2,file='rec.txt',status='unknown')

call rkdump(vstart, nvar, x1, x2, nstep, derivs)

write (*,*) 'done'

end

c  -----
function lowroot(x1, x2, xacc, A, P)
parameter (jmax=20)
rtnewt=x1
do 11 j=1, jmax
call funcd(rtnewt, f, df, A)
dx=f/df
rtnewt=rtnewt-dx
if((x1-rtnewt)*(rtnewt-x2).LT.0)pause 'jumped out of
brackets'
if(abs(dx).LT.xacc) then
P= rtnewt
return
endif
11 continue
pause 'rtnewt exceeding maximum iterations'
end

c  -----
function funcd(x, fn, df, A)

fn= (0.00463)*x*x*x*x*x*x+(0.069458)*x*x*x*x+(0.3472)*x*x-A*x
+0.5786

df= (0.02778)*x*x*x*x*x+(0.277832)*x*x*x+(0.6944)*x-A

return
end

c  -----
function hiroot(x1, x2, xacc, A, P)

```

```

parameter (jmax=20)
rtnewt=.5*(x1+x2)
do 11 j=1, jmax
    call funcd(rtnewt, f, df, A)
    dx=f/df
    rtnewt=rtnewt-dx
    if((x1-rtnewt)*(rtnewt-x2).LT.0)pause 'jumped out of
brackets'
    if(abs(dx).LT.xacc) then
        P= rtnewt
        return
    endif
11    continue
pause 'rtnewt exceeding maximum iterations'
end

c -----
subroutine derivs(x,y,dxdy)
real vt,xthroat,ythroat,Aratio,Mt,T,Md,Mrel,Kd,rhoa,c,rhod,Vd,d,l
real b0,b1,b2,b3,b4,b5,b6,t1,t2,t3,sigma,Vrel,Mrel2,rho,rhoa2
parameter (g=9.8,max=10)
dimension y(max),dxdy(max)

Vd=0.0000000005236
d=0.001
rhod=1000.0
sigma=0.00728

xthroat=4.93
ythroat=0.29546
c    in inches

b0 = 3.9345408511
b1= -2.5940505398
b2= 1.0881241095
b3= -0.327799642
b4= 0.0589415696
b5= -0.0053145754786
b6= 0.00018387291466

l= y(1)*39.37
c    make length into inches

if (l.LT.7.6559) then
+b0    yt= b6*l**(6)+ b5*l**(5)+ b4*l**(4) +b3*l**(3)+b2*l*l +b1*l
else
    yt= 0.5
endif
Aratio = yt/ythroat

if (l.GT.xthroat) then
    call hiroot(1.0, 10.0, 0.001, Aratio, Mt)
else
    call lowroot(0.0000000000000001, 20.0, 0.001, Aratio, Mt)
endif

T= 298/(1+0.2*Mt*Mt)

vt = Mt*sqrt(1.4*287*T)

```

```

Md = y(2)/sqrt(1.4*287*T)

Mrel = abs(Mt-Md)
c write(2,77) y(1), Mt, Md
77 format((F8.3),(F8.3),(F8.3))

t1=(0.3198)+(0.2987)*(Mrel-1)
t2=(0.0809)*(Mrel-1)**(2)
t3=(0.3606)*(Mrel-1)**(3)

if (Mrel.LT.0.5) then
    Kd = 0.192
else
    Kd= t1 - t2 - t3
endif

rhoa =
1.2250/sqrt((1+0.2*Mt)*(1+.2*Mt)*(1+.2*Mt)*(1+.2*Mt)*(1+.2*Mt))

c= Kd*rhoa*d*d/(rhod*Vd)

dxdy(1) = y(2)
dxdy(2) = c*(vt*vt -2*vt*y(2) + y(2)*y(2))
c write(*,*) x, y(1), y(2), dxdy(1), dxdy(2)

c y(3) = Mt-Md

if (Mrel.gt.1.0) then
    Mrel= sqrt((Mrel*Mrel*0.4+2)/(2*1.4*Mrel*Mrel-(.4)))
    rho= 2.4*Mrel*Mrel/(.4*Mrel*Mrel+2)
    rhoa2= rhoa*rho
    vrel= (Vt-y(2))*rho
    y(3)= rhoa2*vrel*vrel*d/sigma
else
    y(3)=rhoa*(Vt-y(2))*(Vt-y(2))*d/sigma
endif

return
end

c -----
SUBROUTINE RK4(Y,DYDX,N,X,H,YOUT)
PARAMETER (NMAX=10)
DIMENSION Y(N),DYDX(N),YOUT(N),YT(NMAX),DYT(NMAX),DYM(NMAX)
HH=H*0.5
H6=H/6.
XH=X+HH
DO 11 I=1,N
    YT(I)=Y(I)+HH*DYDX(I)
11 CONTINUE
CALL DERIVS(XH,YT,DYT)
DO 12 I=1,N
    YT(I)=Y(I)+HH*DYT(I)
12 CONTINUE
CALL DERIVS(XH,YT,DYM)
DO 13 I=1,N

```

```

        YT(I)=Y(I)+H*DYM(I)
        DYM(I)=DYT(I)+DYM(I)
13    CONTINUE
        CALL DERIVS(X+H, YT, DYT)
        DO 14 I=1, N
            YOUT(I)=Y(I)+H6*(DYDX(I)+DYT(I)+2.*DYM(I))
14    CONTINUE
        RETURN
        END

c -----
      subroutine rk4(vstart, nvar, x1, x2, nstep)

      real*8 XX(200), Y(10, 200)
      integer j

      PARAMETER (NMAX=10)
c      COMMON /PATH/ XX(200), Y(10, 200)
      DIMENSION VSTART(NVAR), V(NMAX), DV(NMAX)
      DO 11 I=1, NVAR
          V(I)=VSTART(I)
          Y(I, 1)=V(I)
11    CONTINUE
      XX(1)=X1
      X=X1
      H=(X2-X1)/NSTEP
      DO 13 K=1, NSTEP
          CALL DERIVS(X, V, DV)
          CALL RK4(V, DV, NVAR, X, H, V, DERIVS)
          IF(X+H.EQ.X)PAUSE 'Stepsize not significant in RK4.'
          X=X+H
          XX(K+1)=X
          DO 12 I=1, 3
              Y(I, K+1)=V(I)
12    CONTINUE
13    CONTINUE

      open (unit=1, file='outf.txt', status='unknown')
      do j=1, NSTEP
          write (1, 99) XX(j), Y(1, j), Y(2, j), Y(3, j)
          write (*, *) Y(3, j)
      enddo

99    format((F8.4), (F12.3), (F12.3), (F16.3))
      RETURN
      END

```